Journal of Structural Biology 207 (2019) 136–157

Contents lists available at ScienceDirect

Journal of Structural Biology

journal homepage: www.elsevier.com/locate/yjsbi

Terebratulide brachiopod shell biomineralization by mantle epithelial cells

M. Simonet Roda[a,*], A. Ziegler[b], E. Griesshaber[a], X. Yin[a], U. Rupp[b], M. Greiner[a], D. Henkel[c], V. Häussermann[d,e], A. Eisenhauer[c], J. Laudien[f], W.W. Schmahl[a]

[a] Department of Earth and Environmental Sciences, LMU, 80333 München, Germany
[b] Central Facility for Electron Microscopy, University of Ulm, 89069 Ulm, Germany
[c] Marine Biogeochemistry/Marine Systems, GEOMAR Helmholtz Centre for Ocean Research, 24148 Kiel, Germany
[d] Pontificia Universidad Católica de Valparaíso, Facultad de Recursos Naturales, Escuela de Ciencias del Mar, Avda. Brasil, 2950 Valparaíso, Chile
[e] Huinay Scientific Field Station, Puerto Montt, Chile
[f] Alfred-Wegener-Institut Helmholtz-Zentrum für Polar- und Meeresforschung, 27568 Bremerhaven, Germany

ARTICLE INFO

Keywords:
Transcellular ion transport
Ultrastructure
Amorphous calcium carbonate
ACC
Isotope fractionation
Marine invertebrates

ABSTRACT

To understand mineral transport pathways for shell secretion and to assess differences in cellular activity during mineralization, we imaged with TEM and FE-SEM ultrastructural characteristics of outer mantle epithelium (OME) cells. Imaging was carried out on *Magellania venosa* shells embedded/etched, chemically fixed/decalcified and high-pressure frozen/freeze-substituted samples from the commissure, central shell portions and from puncta. Imaging results are complemented with morphometric evaluations of volume fractions of membrane-bound organelles.

At the commissure the OME consists of several layers of cells. These cells form oblique extensions that, in cross-section, are round below the primary layer and flat underneath fibres. At the commissure the OME is multi-cell layered, in central shell regions it is single-cell layered. When actively secreting shell carbonate extrapallial space is lacking, because OME cells are in direct contact with the calcite of the forming fibres. Upon termination of secretion, OME cells attach via apical hemidesmosomes to extracellular matrix membranes that line the proximal surface of fibres. At the commissure volume fractions for vesicles, mitochondria and lysosomes are higher relative to single-cell layered regions, whereas for endoplasmic-reticulum and Golgi apparatus there is no difference.

FE-SEM, TEM imaging reveals the lack of extrapallial space between OME cells and developing fibres. In addition, there is no indication for an amorphous precursor within fibres when these are in active secretion mode. Accordingly, our results do not support transport of minerals by vesicles from cells to sites of mineralization, rather by transfer of carbonate ions via transport mechanisms associated with OME cell membranes.

1. Introduction

Brachiopods are shell-forming sessile marine invertebrates that have existed from the Early Cambrian and are still extant (e.g. Lowenstam, 1961; Veizer et al., 1986; Peck et al., 1997; Samtleben et al., 2001; Carlson, 2016; Cross et al., 2018). They mineralize low-Mg calcite or Ca-phosphate shells and populate a wide range of marine habitats (e.g. Bates and Brand, 1991; Grossman et al., 1996; Carpenter and Lohmann, 1995; Williams et al., 2000; Cusack, 2001; Peck, 2007; Angiolini et al., 2009; Lee et al., 2011; Roark et al., 2015; Garbelli et al., 2017; Temereva and Kuzmina, 2017).

Brachiopod shells consist of two valves that are connected to each other at the hinge. Unlike mollusc shells each brachiopod valve has a mirror plane, the median plane, that cuts through the valves. The two valves are not mirror images of each other. Brachiopod valves have a quite constant thickness along their length. As juvenile valves are thinner relative to adult ones, valve growth does not occur exclusively at commissural margins, it takes also place along inner shell surfaces (Rosenberg et al., 1988; Baumgarten et al., 2013).

Modern terebratulide and rhynchonellide brachiopod shells consist of up to four shell layers: the outermost periostracum that is followed inward by up to three mineralized layers: the primary, the fibrous and, where developed, the columnar layer. Each shell layer has a specific microstructure (e.g. Schmahl et al., 2004; Griesshaber et al., 2007; Schmahl et al., 2008; Griesshaber et al., 2009; Goetz et al., 2009; Goetz et al., 2011; Schmahl et al., 2012; Gaspard and Nouet, 2016; Ye et al.,

* Corresponding author.
E-mail address: simonet@lrz.uni-muenchen.de (M. Simonet Roda).

https://doi.org/10.1016/j.jsb.2019.05.002
Received 20 December 2018; Received in revised form 2 May 2019; Accepted 4 May 2019
Available online 06 May 2019

2018a,b; Simonet Roda et al., 2019). EBSD measurements show that the primary layer consists of an array of interdigitating, irregularly shaped micrometre sized calcite units (Goetz et al., 2011). Organic substance is not incorporated within the primary layer (Griesshaber et al., 2009). Arrays of calcite fibres form the proximal part of both brachiopod valves. EBSD results prove that the fibrous shell portion consists of sublayers. The latter are formed of differently oriented stacks of parallel calcite fibres (Merkel et al., 2007; Schmahl et al., 2008; Griesshaber et al., 2009). In contrast to the primary layer, in the fibrous shell layer biopolymers are incorporated and are developed as membranes or fibrils (Casella et al., 2018a; Simonet Roda et al., 2019). A thin network of fibrils exists within each fibre (Casella et al., 2018a,b), while organic membranes separate adjacent calcite fibres (Williams, 1966, 1968a,b, 1997). The membranes are secreted only onto the proximal, convex side of the fibres and are not fully encasing them (Simonet Roda et al., 2019). The specific shape and mode of packing of the fibres implicates that they are enveloped by organic substance.

The calcite fibres in modern brachiopods are single crystals (Schmahl et al., 2004; 2008, 2012; Griesshaber et al., 2007; Goetz et al., 2009; Ye et al., 2018a,b). Mild selective etching of these biocrystals produces nanoscale surface morphologies that do not reflect a simple inorganic rhombohedral calcite crystallography, but instead give the appearance of a nanoparticulate mesocrystalline structure consisting of globular units in the 50–100 nm size range (Cusack et al., 2008; Schmahl et al., 2008, 2012; Simonet Roda et al., 2019). For nacre tablets of the gastropod *Phorcus turbinatus* Macías-Sánchez et al. (2017) described as well a globular appearance of the mineral units. However, the authors demonstrated that granularity of the biomineral is not related to the secretion process, but is rather the consequence of the transformation from the precursor to the crystallized mineral. According to Macías-Sánchez et al. (2017) transformation to aragonitic nacre in *Phorcus turbinatus* takes place via an interface-coupled dissolution-reprecipitation mechanism, where, in the presence of water, the original structure of the amorphous mineral is reshaped by the regrowth of the newly-formed crystalline phase. This induces the globular appearance of the crystallized carbonate biomaterial.

Modern rhynchonellide (*Notosaria nigricans* and *Hemithiris psittacea*) and terebratulide (*Laquens californicus*, *Macandrevia cranium*, *Megerlia truncata*, *Terebratalia transversa*, *Calloria inconspicua*; Williams, 1966, 1968a,b, 1997; Williams et al., 2000) brachiopod shell formation was investigated by Williams and co-workers. From TEM and SEM observations the authors deduced a model for shell secretion and proposed that secretory cells of brachiopods are formed within a 'generative zone' of the mantle epithelium: the mantle groove. The latter separates the inner and outer lobes of the mantle edge. Williams postulated (e.g. Williams, 1966) that epithelial cells of the mantle lobes move like 'conveyor belts'. This idea relies on the notion that the generative zone of the mantle epithelium constantly produces new cells, hence, existing cells need to make space and to move away. In agreement with the 'conveyor belt' idea, Williams postulated (Williams, 1966, 1968a,b, 1997) that epithelial cells are capable of performing many secretory tasks and, hence, to secrete all layers of a brachiopod shell: the periostracum, the calcite of the primary layer, the extracellular matrix, the calcite of the fibrous layer and the calcite and extracellular matrix of the columnar shell layer. However, the impetus that is required for the physiological changes that brachiopod epithelial cells must undergo when switching between the many and very different secretory tasks is up to now not determined.

The fibrous and columnar shell layers of modern rhynchonellide and terebratulide brachiopods is a hybrid composite where an extracellular biopolymer matrix is reinforced by calcite. Both material components are secreted by outer mantle epithelium (OME) cells. The organic component is formed within the cells: biopolymers are packed into organelles; these fuse with the apical OME cell membrane and release their content to the shell (e.g. Rothman and Wieland, 1996; Bonifacino and Glick, 2004). For the mineral component two routes of transport from the cell to the site of mineralization might be possible: (1) Transport of material as ions that cross through the cell to the sites of mineralization, or (2) transport of mineral loaded intracellular vesicles that fuse with apical cell membranes and deposit their content at sites of active shell secretion. Despite many decades of cell biological and biochemical research, up to now, there is no definitive evidence whether brachiopod shell mineralization occurs via mineral filled vesicles or by membrane-protein-aided ion transport. Nonetheless, there is general consensus that hard tissue formation occurs under tight cellular control.

Accordingly, the focus of this study is the investigation of brachiopod shell mineralization, in particular, calcite fibre secretion in modern terebratulide brachiopod shells. We started our work with the hypothesis that brachiopod calcite is formed by aggregation of ACC nanoparticles, which are exocytosed by epithelial cells, attach to the developing fibre and crystallize in-situ. Therefore, we conducted an ultrastructural study of outer mantle epithelium (OME) cells that are in direct contact with the growing shell at: (i) the commissure, (ii) central valve sections, and (iii) at and within endopuncta. We describe and visualize ultrastructural differences of the OME at the above mentioned shell regions, substantiate these with quantitative morphometric data of organelle distribution patterns in epithelial cells and propose a conceptual model for mineral transport from OME cells to the sites of calcification. Our starting working hypothesis was not substantiated by our results.

In a broader perspective, we aim with this study for shelled organisms for an up to date understanding of material transport from epithelial cells to the sites of hard tissue formation. This is not only of major importance from a biomineralization perspective. As modern and fossil brachiopods are proxies for climate dynamics and environmental change, it is essential to assess and to evaluate physiological mechanisms that induce fractionation of shell forming isotopes and elements (e.g. Wefer and Berger, 1991; Bates and Brand, 1991; Auclair et al., 2003; Parkinson et al., 2005; Brand et al., 2011). As it has been shown for corals and coccolithophorides, fractionation might arise as a consequence of the mode of material transport to the sites of mineral formation, which is either by ion or by vesicular transport or is possibly a combination of both (e.g. Böhm et al., 2006; Langer et al., 2007; Mejía et al., 2018).

2. Materials and methods

2.1. Materials

In this study we investigated the terebratulide brachiopod *Magellania venosa*. The animals were obtained from Comau Fjord, southern Chile. The brachiopods were taken from 21 m depth, from waters with an average water temperature of 11 °C and 30.3‰ salinity.

Great care was taken that the investigated animals secreted shell material up to the very start of sample preparation. A stock of 150–200 brachiopods were transported live from Comau Fjord, Chile, to GEOMAR, Kiel, Germany, where they were kept in aquaria for three and a half years. In 2018 the brachiopods were transferred to aquaria at AWI in Bremerhaven, Germany, and are still living there today. The brachiopods that were selected for this study lived in the aquaria for more than 6 months prior to the start of sample preparation and had, thus, enough time to adjust to the new living conditions. Within the aquaria the brachiopods were monitored constantly with infrared cameras for observing them opening and closing their valves. Dead animals were discarded immediately. The aquaria were checked for dead animals twice a week.

Brachiopods that we investigated in this study had their valves open. We regard this as a sign that they were constantly filtering, hence feeding and actively secreting shell material. *Magellania venosa* is a fast growing brachiopod. Shell secretion was also checked with the measurement of an increase in shell size, the latter was checked every three

months. The brachiopods adopted well to their new living conditions as they spawned twice per year. Prior to transfer into the fixation solution or preparation for high-pressure freezing it was checked whether the investigated specimens were still alive by having them open and close their valves. Animals that were chemically fixed had a longitudinal axis length between 5 and 7 mm. Brachiopods that were used for high-pressure freezing had a longitudinal axis length of about 4–5 mm. According to Baumgarten et al. (2013), the *Magellania venosa* specimens of the size we used in our study are still juveniles and, thus, have a higher shell growth rate than adults. We investigated in this study eight *Magellania venosa* specimens.

3. Methods

3.1. Chemical fixation and decalcification

For transmission and scanning electron microscopical imaging of the organic phase within the hard tissue and the ultrastructure of mantle epithelial cells we fixed 20 shell pieces that were taken from central shell portions and from the commissure of both valves. All 20 shell pieces contained shell material and adjacent OME. We followed fixation procedures described in Karnovsky (1965) and Seidl and Ziegler (2012). In order to assure best fixation results of the soft tissue we checked the effect of two fixation solutions. The difference between the two fixation solutions was given by the used concentrations of paraformaldehyde and glutaraldehyde. Fixation solution A was prepared by mixing equal volumes of filtered seawater from the culture of *Magellania venosa* containing 2% paraformaldehyde and 2% glutaraldehyde with a solution of 0.35 mol L^{-1} saccharose and 0.17 mol L^{-1} NaCl in 0.2 mol L^{-1} Na-cacodylate buffer (pH 7.7). Fixation solution B was prepared in the same way, however, with higher concentrations of paraformaldehyde (3.2%) and glutaraldehyde (4%) in the filtered seawater. The quality of soft tissue preservation was checked in TEM at 8000 times magnification. We did not find any difference in structure preservation, irrespective which solution was used. Ocassionally we found the OME ruptured or/and slightly detached from the shell. We attribute these features to mechanical impact at shell dissection. These samples were investigated (cut and imaged with FE-SEM and TEM) as well, but were not taken into account for the interpretation of our results. All 20 shell pieces (containing hard and soft tissue) were fixed for 17 h at 4 °C.

Of the 20 specimens, 8, taken from both valves, were decalcified for 14 days in a solution containing 0.25 mol L^{-1} HEPES, 0.05 mol L^{-1}EDTA and 1% glutaraldehyde (Fabritius et al., 2005; Seidl and Ziegler, 2012). The simultaneous decalcification and fixation ensures that the organic matrix emerges slowly, is exposed to the solution and is immediately fixed by aldehyde. Subsequent to decalcification the samples were washed three times with 0.1 M Na-cacodylate buffer (7.7 pH) and postfixed in the same buffer for one hour containing 1% OsO_4 and 0.9% $K_4Fe(CN)_6{\cdot}3H_2O$. After washing with bi-distilled water the samples were dehydrated in an ascending series of isopropanol solutions (30, 50, 70 and 90%) and were contrasted with 2% uranyl acetate (in 100% ethanol for 30 min, washed 3 times for 30 min each in 100% isopropanol and two times for 5 min in propylenoxid).

Finally all 20 shell pieces were embedded in EPON resin and were cut with an ultramicrotome for imaging in TEM and FE-SEM as thin sections or as block-faces, respectively.

3.2. High-pressure freezing and freeze-substitution

High-pressure freezing enhances significantly the quality of morphological preservation of soft tissue samples for electron microscopical observation (Giddins, 2003). *Magellania venosa* not larger than 6 mm in length were dissected in the seawater of the culture. Pieces of shell with the mantle epithelium attached to the shell were cut from the commissure and the central shell portion of both valves. Samples were transferred to hexadecane and placed in aluminium planchets with an outer diameter of 3 mm and a 200 μm deep cavity, and covered with the flat side of another planchet. Samples were then high-pressure frozen with a Wohlwend HPF Compact 01 high-pressure freezer within 30 ms at a pressure of 2.3×10^8 Pa.

Some of the high-pressure frozen samples were, in addition, subsequently freeze-substituted. The substitution medium enhances further ultrastructural features of biological soft tissues (Walther and Ziegler, 2002). The planchet sandwiches were opened and freeze-substituted overnight in 0.2% OsO_4, 0.1% uranyl acetate and 5% H_2O in acetone from −90 °C to 20 °C following the protocol described in Walther and Ziegler (2002). Finally, the samples were embedded in EPON resin and cut by using a diamond trimming knife (Diatome) and a Reichert Ultracut ultra microtome.

In a further procedure some of the high-pressure frozen, freeze-substituted and EPON embedded samples were decalcified for two weeks with 0.25 mol L^{-1} HEPES, 0.05 mol L^{-1} EDTA. The samples were then re-embedded in EPON. This procedure facilitated better thin sectioning for TEM imaging.

In order to visualize simultaneously epithelial cells, organic matrices and shell mineral with FE-SEM we used chemically fixed but non-decalcified as well as high-pressure frozen and freeze-substituted samples, all of them embedded in EPON resin. Samples were mounted on 3 mm thick cylindrical aluminium rods using super glue, were cut (Reichert Ultracut ultramicrotome) with glass and polished with diamond knifes (Diatome). Samples were then coated with 4 nm of carbon and imaged with a Hitachi S5200 FE-SEM. After imaging the carbon layer was removed, sample surfaces were re-polished, etched and fixed simultaneously for 40 s with a solution containing 0.1 M HEPES (pH = 9.0) and 2.5% glutaraldehyde. Samples were then treated with 100% isopropanol 3 times for 10 s each and critical point dried in a BAL-TEC CPD 030 devise. After coating with 4 nm carbon the dried samples were imaged again with a Hitachi S5200FE-SEM.

3.3. Sample preparation for microstructure characterisation

Electron Backscatter Diffraction (EBSD) measurements were done on even surfaces of high-pressure frozen and freeze-substituted samples, embedded in EPON resin. The used sample preparation for high-pressure freezing, freeze-substitution and embedding in EPON is described in the sections above. For the required even surfaces, samples were cut and polished with a diamond microtome knife and were subsequently coated with 4–6 nm of carbon.

3.4. Transmission electron microscopy

Ultrathin 60 nm thick sections were cut from chemically fixed and high-pressure frozen and freeze-substituted and decalcified samples using a diamond knife and an ultramicrotome. The sections were placed on carbon stabilized Formvar-coated copper hole grids and stained with 0.3% lead citrated.

A Zeiss 912 TEM equipped with an Omega energy filter, a goniometer stage and a 2 k × 2 k pixel camera was used to image the sections at 8000 times magnification and 120 kV acceleration voltage using only elastically scattered electrons. To screen a large area of the outer mantle epithelium at high resolution, up to 60 panorama images were recorded at rectangular grids, each of these containing between 250 and 300 high-quality individual images. These were then aligned using the TRS software and formed the composite panorama images. Up to 20 composite images were used for structural and numerical analysis.

3.5. Field emission scanning electron microscopy

Non-decalcified animals were chemically fixed as a whole (Fabritius and Ziegler, 2003, Fabritius et al., 2005). Small pieces of the shell were embedded in EPON resin and knife polished with successively

advancing the knife to the surface of the sample to 70, 40, 20, 10 and 5 nm, repeating each polishing step 15 times. Samples were mounted on aluminium holders using self-adhesive carbon pads and conductive glue and were coated with 4 nm of carbon using a BAF 300 BAL-TEC coating mashine. Samples were analysed with a Hitachi S5200 field emission scanning electron microscope (FE-SEM) using the converted backscattered electron signal to obtain so called composite rich images (Walther, 2008) with 20 µA emission current and 4 kV acceleration voltage in analysis mode of the microscope. Secondary electrons from the sample were suppressed by 100% so that only the backscatter electron signal was used for imaging.

3.6. Electron backscatter diffraction

EBSD measurements were carried out on a Hitachi SU5000 field emission SEM, equipped with an Oxford EBSD detector. The SEM was operated at 15–20 kV and measurements were indexed with the CHANNEL 5 HKL software. In this study crystal orientation information is presented with band contrast measurement, colour-coded crystal orientation images and corresponding pole figures. EBSD band contrast represents the pattern quality of the EBSD-Kikuchi diffraction pattern, where a strong EBSD signal yields a bright image point when a crystal is scanned. An absent signal results from organic material or the presence of amorphous mineral. Co-orientation statistics are derived from pole figures obtained from EBSD scans. A measure of crystal co-orientation is given by the MUD value, a value defined as the multiple of uniform (random) distribution. Thus, high MUD values indicate a high crystal co-orientation, whereas low MUD values reflect a low to random co-orientation, respectively. For further information see Griesshaber et al. (2013, 2017), Casella et al. (2018a,c).

3.7. Morphometry

In this study we aim for a comprehensive understanding of the ultrastructure of OME cells that are in close contact with the growing shell. We investigate the relation between OME cells and actively secreted calcite fibres. Accordingly, our intention was to image large portions of the OME with very high quality TEM and SEM images and perform a statistical evaluation of organelle distribution patterns for a large portion of the OME. To achieve the latter we recorded 60 TEM panorama images. Each panorama image covered both, shell calcite and OME cells and consisted of 250 and 300 individual very high-quality TEM images. The individual TEM images were aligned to each other and formed the TEM panorama images. Of these 60 panorama images we selected 18 for numerical analysis. Of the 18 panorama images we selected 48 areas of interest, with each area of interest covering many OME cells depicted in very high resolution. The statistical evaluation was performed for two animals. We did not perform the statistical evaluation in 3D, as the intention was to cover large portions of the OME. A 3D statistical evaluation is carried out currently in a further study. OME volumes are selected on the basis of our imaging and statistical results obtained from the 2D statistical evaluation.

Throughout this study we compare for the central shell region two types of outer mantle epithelia:

OME that is connected by hemidesmosomes within the apical OME cell membrane to the extracellular organic membrane lining at the proximal convex surface of the fibres. We use the abbreviation *cr-a: central shell region with OME – attached*.

OME where both the extracellular organic membrane at the convex proximal side of the fibres as well as the apical hemidesmosomes are absent. In this case the apical cell-membrane delineates the compartment into which the cell secretes all components of the shell-forming mineral. We use the abbreviation *cr-s: central shell region with OME – secreting*. For further description see Simonet Roda et al. (2019). These two epithelia alternate at about the cross-sectional size scale for a calcite fibre, i.e. at about 7–9 µm.

We also examined the *thin epithelium at the puncta (pt)* and regard it as an epithelium that is not involved in mineral secretion. We consider the epithelium at and within the puncta as a reference the secreting epithelia.

Furthermore, we compare the multi-cell layered OME underneath the calcite fibres at the inner commissure (*abbreviation: com*) with the single-cell layered OME below central shell regiona (*abbreviation: cr-all*).

Volume fractions of various organelles were determined by counting randomly positioned points on predefined structures (classes) within test fields using the open source software JMicroVision Image analysis system (Roduit, 2008). Twelve different classes were defined as: *cytoplasm, nucleus, mitochondria, lysosomes-endosomes, vesicles, Golgi apparatus, rough endoplasmic reticulum, smooth endoplasmic reticulum, glycogen, multivesicular bodies, others, and extracellular space.* The number of random points was set either to 250 or 500 depending on the size of the test field. Test areas were defined using the implemented "area editor" so that regions outside of the epithelium were at a minimum. Evolution plots created by the software were used to evaluate if calculated volume fractions of organelles are representative.

For each test field the length of the epithelium "E_L (µm)" and the test field area "A_T (µm^2)" were determined and the percentages of the various classes "A_p (%)" in "A_T" were measured.

The absolute area "A_O(i)" of each class i was calculated by

$$A_O(\mathrm{i}) = A_T * (A_p(\mathrm{i})/100)\ (\mu m^2)$$

The areas of the extracellular space and of the nucleus were excluded by calculating the area of the cytoplasm "A_C" within the test field by

$$A_C = \left(\sum_{(classes\,i=1)}^{1} A_O(i)\right) - A_O(\mathrm{nucleus}) - A_O(\mathrm{extracellular\ space})(\mu m^2)$$

The volume fraction of each class "V_O(i)" of the cytoplasm without the nucleus equals the area fraction "A(i)" and was calculated by

$$V_O(\mathrm{i}) = A(\mathrm{i}) = (A_O(\mathrm{i})\ /A_C) * 100\ (\%)$$

From the area fraction "A(i)" of classes i, we calculated the absolute volume V_A(i) of classes i per 10 µm^2 epithelium area by

$$V_A(\mathrm{i})\ (\mu m^3/\mu m^2) = A_O(\mathrm{i})/E_L * 10\ (\mu m^2/\ \mu m)$$

For measuring the area of cell membranes as well as for the outer membrane of the mitochondria we followed the method of Merz (1967). As the region of the OME near the shell rim (commissure) contains numerous long extensions it was not possible to distinguish the apical cell membrane from the basal one. Therefore, we distinguished a distal from a proximal cell membrane, with the latter most probably containing both apical and lateral membrane compartments. The Merz grid plugin for ImageJ/Fiji (Research Services Branch, National Institute of Mental Health, Bethesda, MD, USA) was used to superimpose an array of coherent semicircular lines to the images. The profile length "L_p" of the cell membrane and the outer membrane of the mitochondria was determined by counting the intersections of the Merz grid lines with the membranes inside the test fields. L_p was calculated by:

$$L_p = N\ d(\mu m)$$

with "N" as the number of intersections between the grid lines and the membranes and "d" the diameter of the semicircles in each test field.

L_p was normalized to 1 µm epithelium length by

$L = L_p/E_L$ with "E_L" the epithelial length within the test field.

The areas of the membranes "A_M" per µm^2 area of epithelium was calculated by

$A_M = L \times 1.273$ (µm^2) (Merz, 1967).

3.8. Statistical analysis

GraphPad Prism software, version 6.00, for Mac (GraphPad Software, La Jolla California USA, www.graphpad.com) was used for statistical analysis and graphical representation. Mean values and standard deviations were calculated for the volume fractions $V_O(i)$, the absolute volume of each class normalized to 10 μm^2 of epithelium V_A, and the membrane areas normalized to one square micrometer epithelium A_M for the distal and proximal cell membrane, and the outer membrane of the mitochondria. One way ANOVA was used to test the significance of differences in the mean values for the volume fraction $V_O(i)$ and area per 10 μm epithelial length of classes $A_O(i)$. To account for multiple comparisons, Sidiaḱs multiple comparisons tests were used to assign significant differences between the mean values for the mineral secreting central region (cr-s), the non-secreting attached areas (where the OME is attached to the organic membrane at the convex proximal side of the fibre) of the central shell region (cr-a) and the puncta (pt). T-tests were used to test for significant differences between the mean values of the pooled central regions.

4. Results

4.1. The shell

The schematic presentation shown in Fig. 1 depicts the different layers of the shell of modern *Magellania venosa* as well as the topological relation of the mantle epithelium to the growing shell. The scheme is true to scale for an approximately 10 mm large *Magellania venosa*. Fig. A1 indicates on cross-sections through the two valves those shell portions that were investigated in this study: the commissure and the central shell region (Fig. A1B).

The valves of *Magellania venosa* (Fig. A1 A) consist of an outer organic layer, the periostracum, and two mineralized layers, the primary and the fibrous shell layers. The periostracum in *Magellania venosa* (Figs. 1, 2A) is a reticular structure that contains thin branching septae and large hollow spheres, the latter being similar to those observed in the periostracum of the bivalve *Mytilus edulis* (Wählisch et al., 2014). Along the proximal side of the periostracum, small spherical structures with a dense (osmiophilic) core fuse with one another. At its distal side the reticular structure of the periostracum is connected to a flat and thin sheet that carries numerous small rods (Fig. 2A) and is interrupted by large pores (Fig. 2A). At its proximal side the periostracum of *Magellania venosa* is lined by a porous basal layer (red rectangles in Fig. 2A), hence, there is access from an outer medium to the puncta.

The primary shell layer (Fig. 1), is secreted at the outer commissure (Simonet Roda et al., 2019) and consists of micrometre sized, irregularly shaped, interdigitating calcite units (Goetz et al., 2011). In a 10 mm long *Magellania venosa* shell, secretion of fibres (Fig. 1) starts about 100 μm away from the outer commissure. The fibrous shell layer has a plywood structure as it comprises differently oriented stacks of parallel-assembled calcite fibres (this study and Goetz et al., 2009, Griesshaber et al., 2009, Schmahl et al., 2012). A brachiopod fibre has in cross section four sides: one convex proximal side and three concave sides, the latter located distally or laterally (Fig. A2A, Simonet Roda et al., 2019, Ye et al., 2018a,b). Each fibre is lined by an organic membrane, however, only at its convex, proximal surface (Simonet Roda et al., 2019). TEM micrographs of high-pressure frozen and decalcified samples show occasionally branching of organic membranes at lateral fibre corners (Fig. 2B, C, A2C to A2G). This takes place when a new membrane attaches to a pre-existing membrane, resulting in double-plied membrane sections in many but not all cases. Since the membrane has only one open margin per double-plied membrane corner, an artefactual origin of the branching, e.g. by rupturing the membrane apart during sample preparation, can be excluded. In *Magellania venosa* the extracellular organic membrane is porous; porosity becomes well visible when the membrane is sectioned tangentially (Fig. 2D and Nindiyasari et al., 2015, Griesshaber et al., 2017).

4.2. The mantle epithelium

The mantle epithelium in *Magellania venosa* (Fig. 1) consists of an **outer** (OME, Figs. 3–11) and an **inner** (IME, Figs. A3, A4) section. Based on ultrastructural differences we are able to distinguish between the outer mantle epithelium that is present at the **commissure** (mainly below the primary layer and the first few rows of fibres, Figs. 1, 4–7, A3–A6) and the epithelium at **central shell portions** (here, only below the fibres, Figs. 1, 8–10, A7). Moreover, **within the commissure**, we differentiate between the OME at the **outer commissure**, an OME section where we cannot distinguish between OME cells and IME cells on the basis of their ultrastructural characteristics (Fig. 1A), and the OME at the **inner commissure** where the OME and IME are separated by a haemolymph space (Fig. 1A).

At the commissure the OME is multi-layered, while below central shell portions it is single-layered (Fig. 1A). In an about 10 cm long *Magellania venosa* shell, the transition from multi-layered to single-layered OME is about 350–400 μm away from the tip of the shell (Fig. 1A). At the commissure and below the first row of fibres the thickness of the OME can exceed 30 μm (Fig. 1B). It is thicker than the mantle epithelium underneath the primary layer at the very tip of the commissure (Fig. 1A, B). At the inner commissure, within the multi-layered OME portion, the thickness of the fibrous layer is about the same as that of the primary layer (white arrows in Fig. 1A). This indicates that mineral deposition in this part of the commissure has similar rates for both the primary and the fibrous layers, respectively. When secretion of the fibres starts the thickness of the primary layer cannot be changed any more. With increasing distance x from the commissure (Fig. 1A), the thickness d of the fibrous layer increases, however, towards the central shell regions the corresponding thickness increment ($\Delta d/\Delta x$) decreases. This indicates that the rate in mineral deposition (biomineral formation per time increment) decreases from the commissure to central shell regions. In *Magellania venosa* the angle between the fibres and the OME is about 10°.

4.3. The mantle epithelium at the commissure

Figs. 3 to 7 and A3 to A6 show ultrastructural features of the OME at the commissure. The periostracum and the primary shell layer are secreted at the outer commissure (Figs. 3, 4A, B). OME cells consist here of long cell extensions and are devoid of cell bodies containing a nucleus (Figs. 1B, 3, 4A). We distinguish between distal and proximal cell extensions (Fig. 4A). Distal extensions are close to the calcite of the primary layer, and are devoid of cell organelles such as endoplasmatic reticulum, Golgi apparatus or mitochondria, but contain numerous very dense spherical bodies with 300–400 nm in diameter (sb in Fig. 4A). Proximal extensions (Fig. 4A) are in the vicinity of the forming periostracum (Fig. 4B). Although the content of organelles of proximal extensions is similar to that of the distal ones, dense spherical bodies in the proximal extensions are more irregular in shape and density. Distal and proximal extensions are separated from each other by a layer of degraded cell extensions (dce in Figs. 4A, 3) that contain much cell debris.

The periostracum is secreted at the proximal side of the mantle epithelium by proximal cell extensions (Figs. 3, 4A, B). It develops within a shallow pouch of the epithelium (outlined with a yellow dashed line in Fig. 4B) and is covered by a layer of irregularly distributed material, most likely consisting of mucous polysaccharides (blue star in Fig. 4B). Within the pouch at the beginning of the periostracum irregular and partly dense secretions can be observed (yellow star Fig. 4B). Dense or osmiophilic material lies extracellularly between the tips of two extensions and the basal layer (red arrows in Fig. 4B) of the periostracum.

Cell extensions below the primary layer have their origin in cell

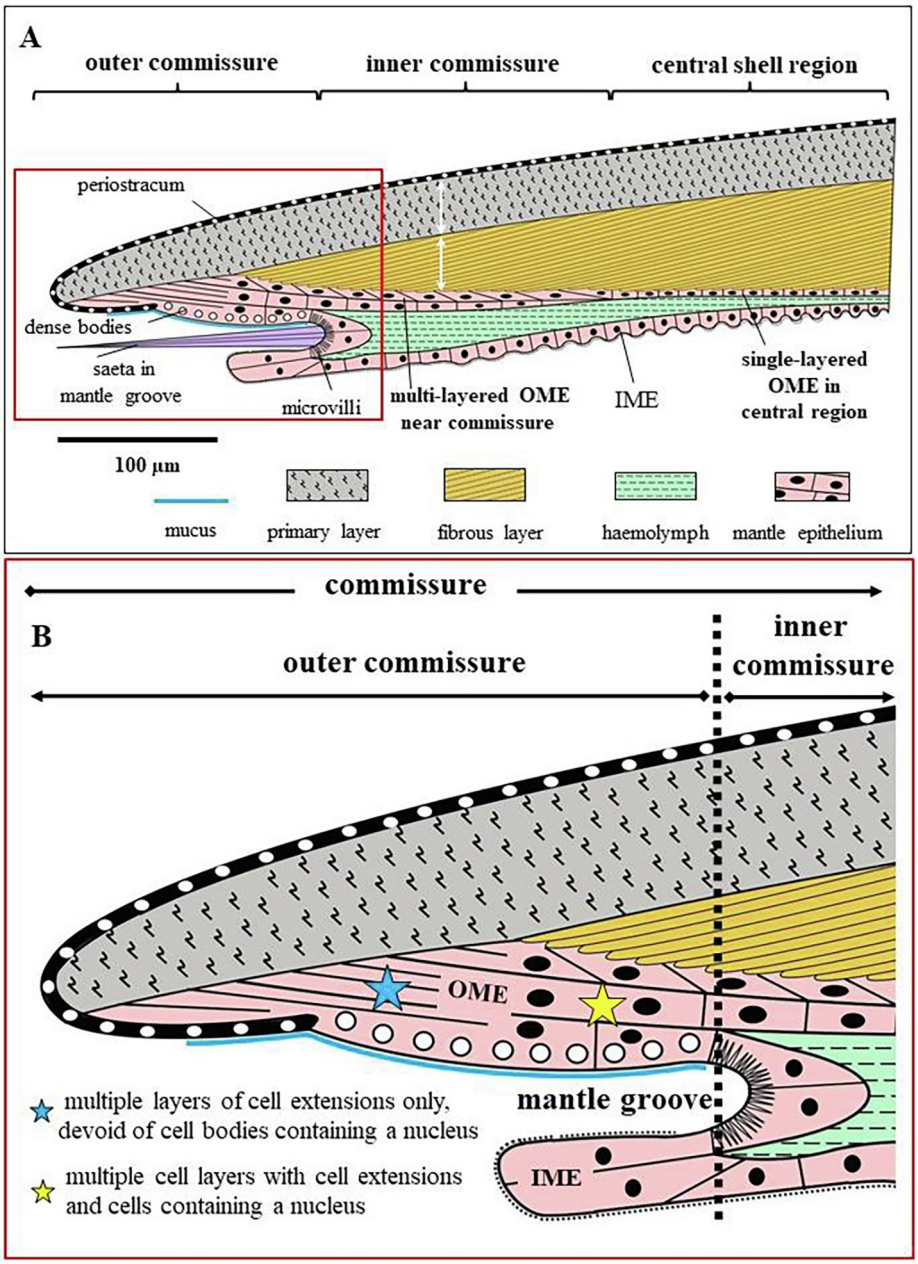

Fig. 1. Scheme showing the different layers of the shell of *Magellania venosa* and the topologic relation between the mantle epithelium and the shell. The scheme is true to scale for a 10 mm large specimen. A) The shell of *Magellania venosa* consists of three layers, the periostracum, the mineralized primary layer and the mineralized fibrous (secondary) layer. The mantle epithelium is subdivided into two regions: the outer (OME) and inner mantle epithelium (IME). B) Region of the commissure enlarged from A (red rectangle in A). Based on ultrastructural characteristics we can distinguish different portions of the OME: (i) the OME at the outer commissure below the primary layer, (ii) the OME at the outer commissure below the first row of fibres, (iii) the OME at the inner commissure below the fibres and (iv) the OME below central shell portions. Within the commissure the OME is multi-layered, while at the central shell region the OME consists of a single layer of cells. For an about 10 mm large *M. venosa* the transition from multi-layered to single-layered OME is about 350–400 µm away from the tip of the commissure. The OME at the outermost portion of the commissure at the primary layer consists of cell extensions (blue star) only, while, still within the outer commissure but below the fibres, the OME consists of cell extensions and cells with a nucleus (yellow star).

bodies that contain a nucleus and are situated in the multi-cellular portion of the mantle epithelium (blue and yellow stars in Fig. 1B, right-hand upper part of Fig. 4C). This part of the multicellular region (the part of the OME at the outer commissure where cell extensions contain a nucleus) is close to the site where the secretion of fibres starts (Figs. 4C, 1). Due to the absence of a mantle cavity or an extracellular matrix a clear borderline between the OME and IME is not observable (Figs. A3, 4C). Close to the appearance of fibres the mantle epithelium forms a grove (Fig. 3). At the base of the latter setae are formed (Figs. 1, A3). From the tip of the commissure to the base of the mantle groove a 400 nm thick mucus layer covers the periostracum (black arrows in Figs. 3 and 4A and B).

The inner mantle epithelium (IME) begins proximal of the mantle groove (Figs. 1, A3, A4). It consists of a single layer of cells that carry numerous microvilli like extensions and cilia at their apical side (Fig. A4). IME cells contain many large dense bodies and organelles of the lyso-endosomal pathway of varying sizes as well as endoplasmic reticulum and many mitochondria (Figs. A3, A4).

The OME at the commissure underneath the first few fibres (Figs. 1B, 3, 4C) is characterized by many cell extensions and by elongated cells containing a nucleus. This is in contrast to the OME at the very outer commissure, which consists of cell extensions only; OME cells here secrete solely the primary layer of the shell. The cell extensions below the fibres run obliquely towards the tip of the commissure and attach with their distal ends to the fibres (Figs. 5A and 6A). Within the commissure, but below the fibres (Fig. 6C), the mantle epithelium is zoned. We distinguish a distal zone, an inner zone, a proximal zone and a dense body zone (Figs. 4C, 5A, 6A). Within the commissure, but where OME and IME are separated by hemolymph space, we also find a zonation, however, here the dense body zone and the mucus layer are lacking (Fig. 7A).

The **distal zone** (dz, in Figs. 5A, 6A, 7A) consists of the outermost layer of cellular extensions. Cellular profiles are flat, are up to about 1000 nm thick and line the convex proximal side of the fibres (Figs. 5A, B, 6A–C, 7A). We often observe very thin cells at these cellular extensions (e.g. Figs. 5B, 6B, C, 7A). In most cases, more than one cellular

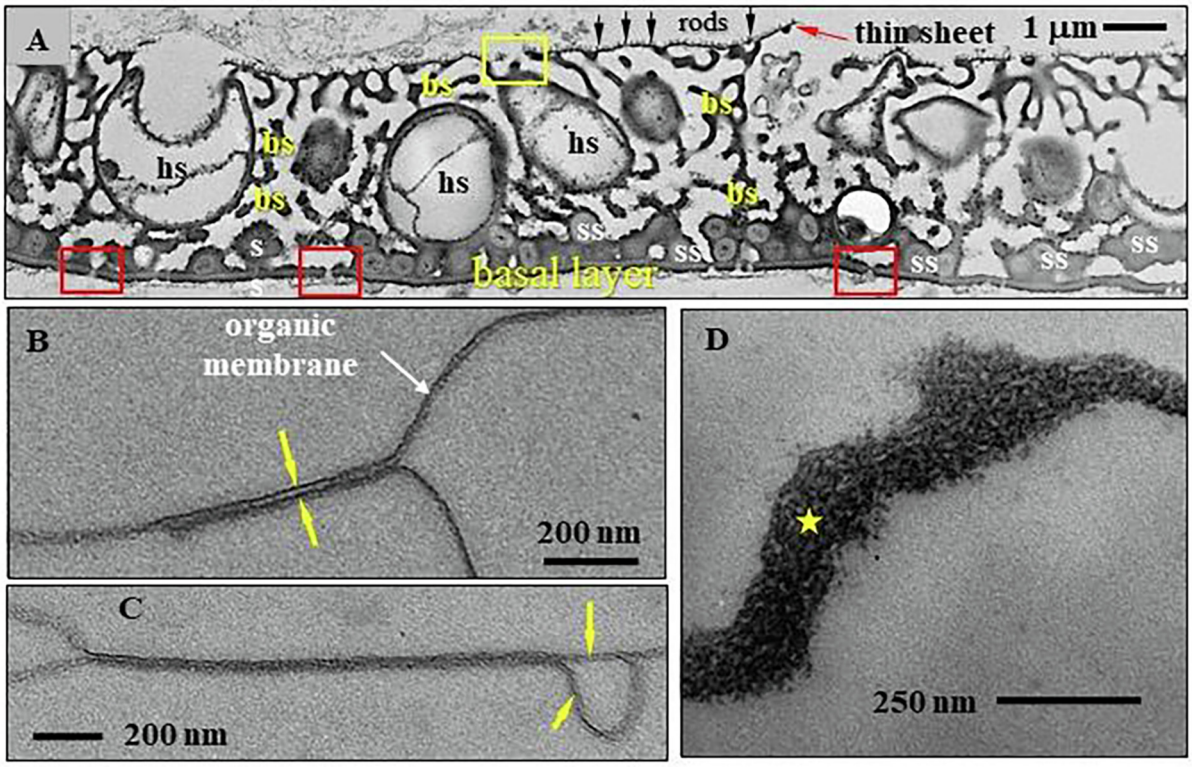

Fig. 2. TEM micrographs showing ultrastructural features of the periostracum (A), and the fibrous shell layer (B to d) of *Magellania venosa*. A) Periostracum of a chemically fixed and decalcified sample. Thin branching septae (bs) form a reticular structure interrupted by large hollow spheres (hs). In the proximal area, small osmiophilic spherical structures (ss) fuse with one another and with a basal layer of the periostracum. The basal layer contains small pores (red rectangles). Apically the periostracum has a thin flat sheet that carries numerous small rods at its distal side (black arrows) and is interrupted by large pores (yellow rectangles). B, C) Often two organic membranes overlap at fibre corners (for further information see Fig. A2). D) Tangential cut through an organic membrane between two fibres showing the porosity of these membranes.

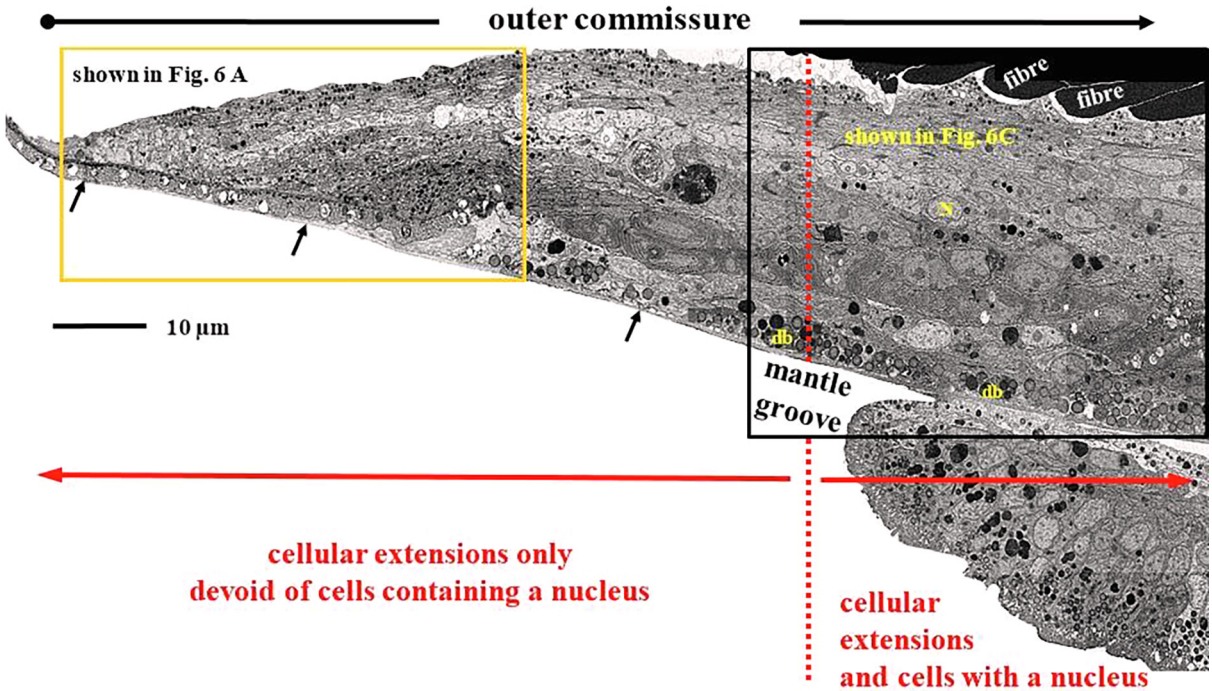

Fig. 3. FE-SEM panorama image (aligned sequence of micrographs) of an embedded and polished sample depicting the outer mantle epithelium (OME) at the **outer commissure below the primary shell portion and the first rows of fibres**. The contrast is reversed. The red arrow pointing to the left indicates OME portions that consist of cellular extensions only present at the outermost part of the commissure. Towards inner commissure regions (red arrow pointing to the right) the OME contains cellular extensions as well as cells having a nucleus (N). At inner commissure regions there is a high abundance of dense bodies (db) at the proximal side of the OME. Subimages of Fig. 5 are shown in Fig. 6A and C, respectively. Black arrows point to the presence of a mucus layer.

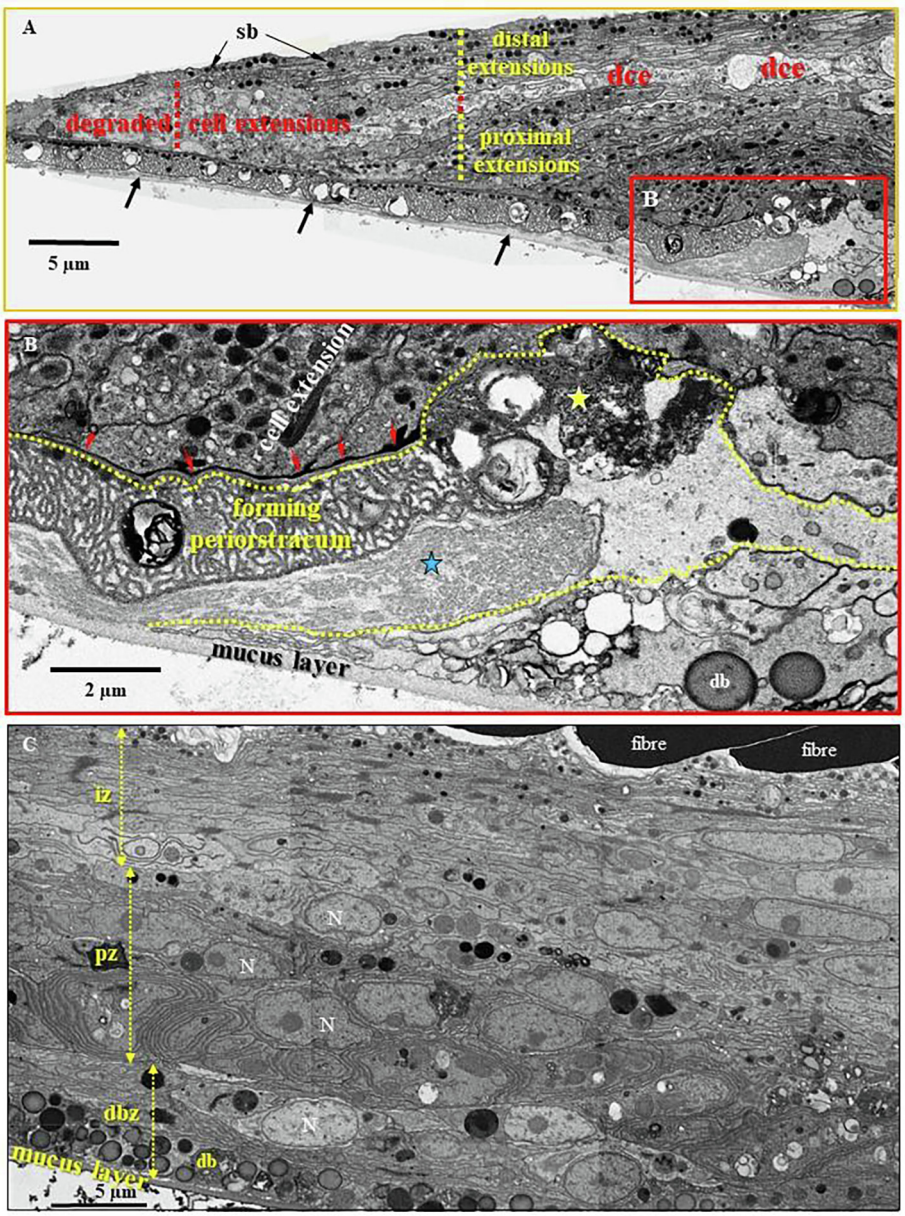

Fig. 4. FE-SEM micrographs of embedded and polished samples depicting the outer mantle epithelium (OME) at the **outer commissure**. The contrast is reversed. A) Detail, marked with an orange rectangle in Fig. 5, consists of cell extensions, distal at the primary layer and proximal near the periostracum. Between these is a region formed of degraded cell extensions (dce). Small dense bodies (sb) are present at proximal and distal extension sites. B) Zoom into the region that is marked with a red rectangle in A, depicting the site of periostracum formation within a shallow pouch (outlined with a dashed yellow line in B). Dense extracellular material occurs between the periostracum and the OME. Red arrows in (B) point to the basal layer of the periostracum. Blue star in B: mucus material close to the forming periostracum; yellow star in B: irregular and partly dense secretions close to the forming periostracum. C) Multi-cellular mantle epithelium below fibres at the outer commissure. Due to ultrastructural differences we distinguish different regions within the epithelium: the apical zone (az) consists of thin cell extensions only; the inner zone (iz) consists of larger extensions; the proximal zone (pz) contains cells with a nucleus (N) and the distal proximal zone (dbz) contains many large dense bodies (db) in addition to cell bodies with a nucleus.

profile occurs directly below a single calcite fibre (e.g. Fig. 5B). Organelles in the distal zone are rare (Figs. 5A, 6A, 7A). OME cells are connected to organic membranes of the fibres via apical hemidesmosomes (Fig. 7B). These are abundant, are very small and can be seen best in obliquely cut sections as dense plaques (black arrows in Fig. 7B). In regions where an organic matrix is absent cell extensions are always covered with a thin surface coat (black arrows in Fig. 7C). Adherence junctions resembling adhesion belts connect apical cell extensions with each other (Fig. 7D). In high-pressure frozen and freeze-substituted shell and polished samples we see that OME cells are in very close contact with the calcite of the fibres (Fig. A5 and in more detail see Simonet Roda et al., 2019).

Within the ***inner zone*** (Figs. 4C, 5A, 6A, 7A), cell extensions and the shape of most of the cell profiles are round in cross section (Figs. 5B, 6C) and their thickness increases from the the distal zone towards the proximal side of the inner zone (Figs. 5A, 6A, 7A). In the proximal part of the inner zone lysosomes are the most common organelles, rough endoplasmic reticulum and vesicles are present but not as common, while mitochondria, multivesicular bodies and Golgi stacks are very rare. In most cases cell extensions are devoid of nuclei (Figs. 5A, 6A, 7A). Widened intercellular spaces filled with electron dense material are common and occasionally contain extracellular vesicles (yellow circles in Fig. 7E).

Within the ***proximal zone*** (Figs. 5A, 6A, 7A) we find cell bodies that contain a nucleus. Cells here are elongated in horizontal direction and have round profiles in cross section. In addition to nuclei, cells within the proximal zone are very rich in organelles, in particular mitochondria, long cisternae of rough endoplasmic reticulum, Golgi apparatus and organelles of the endo-lysosomal pathway including multivesicular bodies (Figs. 4C, 5, 6, 7). Smooth endoplasmic reticulum and glycogen are rare. The cells are connected to each other by gap junctions (Figs. 7, 10).

The ***most proximal, dense body zone*** occurs only in the *outer commissure* and is formed of cells containing many large and spherical dense bodies (***dense body zone***, dbz in Figs. 4C, 5A, 6A). In the dense body zone the apical side of the cells faces seawater. Spherical dense bodies occur only between the end of the pouch where the periostracum is secreted and the base of the mantle groove just above the mucus layer. Near the base of the mantle groove the epithelium separates into the outer and the inner mantle epithelium. The dense body layer is

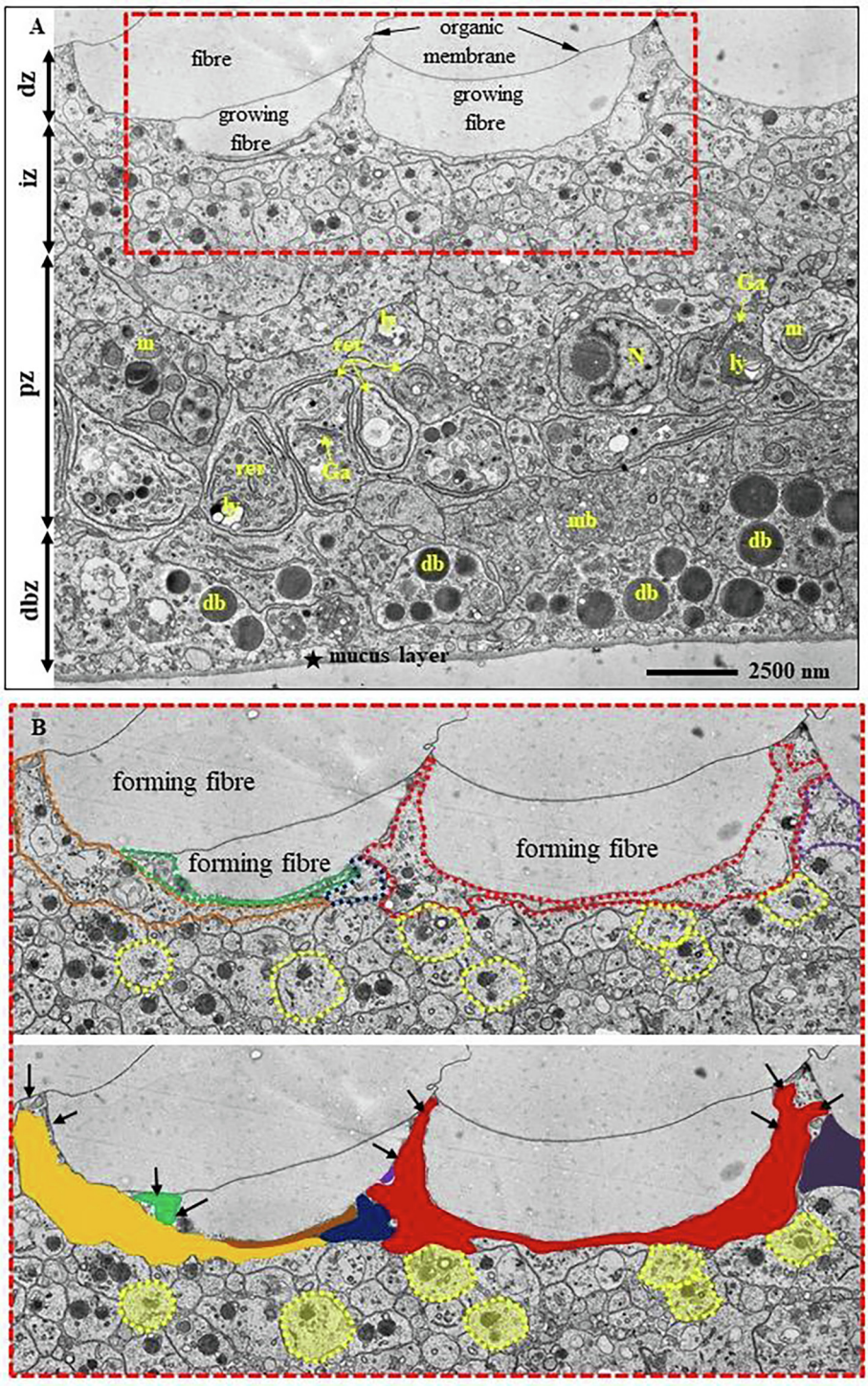

Fig. 5. TEM micrographs of a chemically fixed and demineralized sample depicting a perpendicular cut through fibres, cells and cellular extensions at the **outer commissure**. A) Four regions can be distinguished: The distal zone (dz), the region that is in contact with the fibres consists of small extensions; organelles are absent. Within the inner zone (iz) of the epithelium cellular extensions increase in size and contain organelles such as Golgi apparatus (Ga), mitochondria (m) and rough endoplasmic reticulum (rer). The proximal zone (pz) contains many cell bodies; organelles are abundant, especially nuclei and mitochondria. The most proximal zone (dbz) is characterized by the presence of dense bodies (db). Ly: lysosome; mb: multivesicular body. B) A cell extension is attached to a few fibres, e.g. for the cell outlined in red in to 5 fibres. The shape of the cell extension that is in direct contact to the growing fibre adapts to the profile of the fibre, while further below cell extension profiles are round (outlined in yellow in B).

continuous with the inner mantle epithelium.

4.4. The mantle epithelium at central shell regions

In a 10 mm long *Magellania venosa* shell, about 350–400 µm away from the tip of the commissure, the OME changes from a multi-layered to a very thin single-layered epithelium (Fig. 1A). Cell thicknesses vary, even within a single cell (Fig. 8 A to E, A7). In thick cell portions, the OME is about 1–3 µm thick and organelles such as the nucleus, mitochondria, rough endoplasmic reticulum and glycogen are abundant. Neighbouring cells form extended interdigitations between each other (Fig. 9), resulting in an increase of the basal plasma membrane surface area. Many gap junctions between cells can be observed (Fig. 7F, Fig. 10A, B, C).

However, cells at central shell regions can also be extremely thin, as thin as 20 nm (Fig. 8D, E, F). In these cases they are devoid of cell organelles (Fig. 8C, D, E, A7) and are mainly below shell portions where the organic membrane of the calcite fibres is not yet developed (Fig. 8C, D), thus at sites of active shell secretion. In addition, these thin cells at these sites are covered by a surface coat (Fig. 8E).

Thick cells or cell portions are connected to the organic membrane that lines the proximal convex surface of fibres via hemidesmosomes

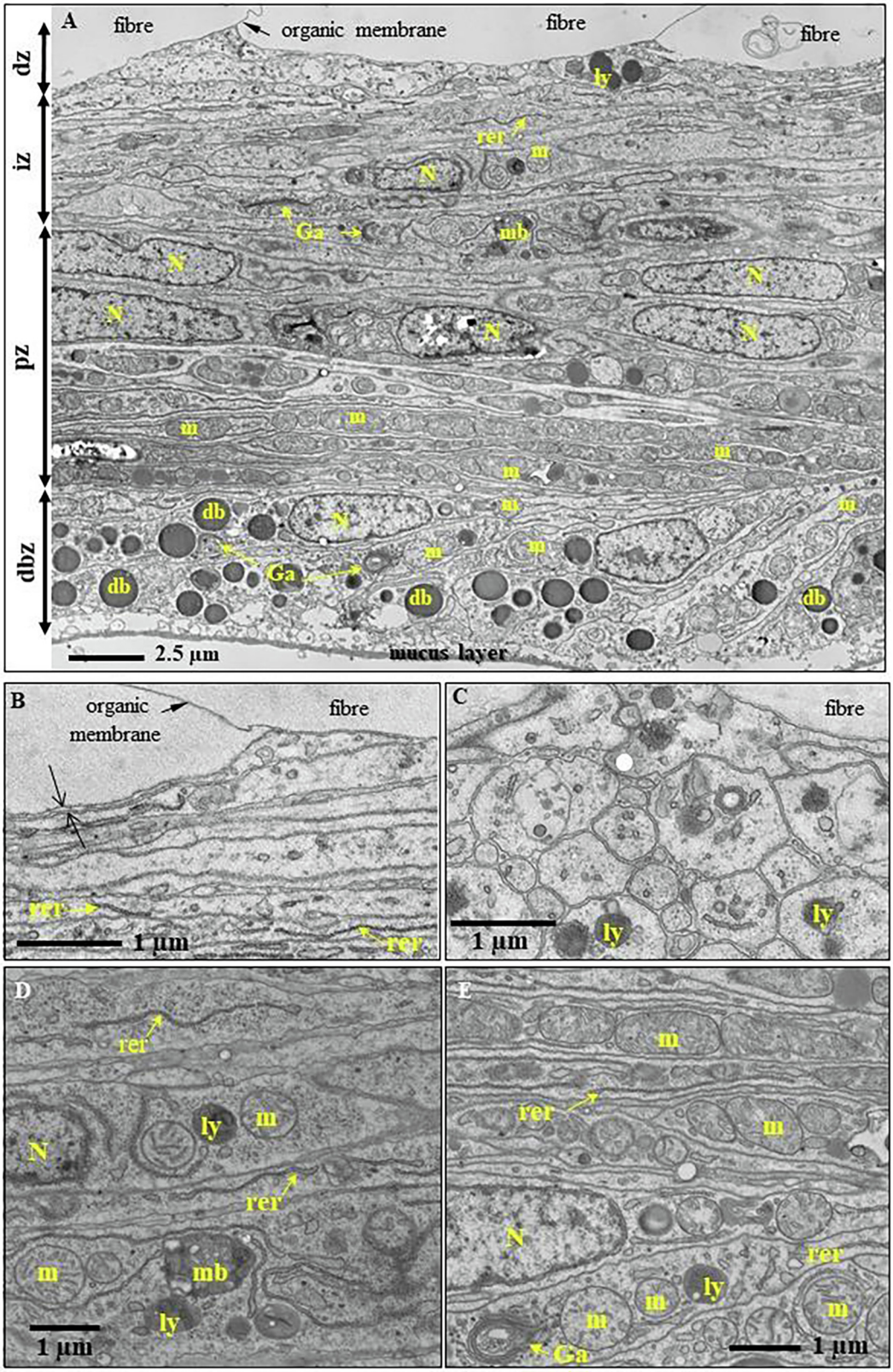

Fig. 6. TEM micrograph of chemically fixed and demineralized samples depicting fibres, cellular extensions and cells at the **outer commissure**. A) Calcite fibres are cut in longitudinal direction. Within the epithelium we distinguish four different regions: the distal zone (dz), the region that is in contact with the fibres consists mainly of small extensions; organelles are rare. Within the inner zone (iz) of the epithelium cellular extensions increase in size and contain organelles such as Golgi apparatus (Ga), mitochondria (m) and rough endoplasmic reticulum (rer). The proximal zone (pz) contains many cell bodies; organelles are abundant, especially nuclei and mitochondria. In the most proximal zone (dbz) dense bodies (db) are abundant. B), C), D), E) TEM micrographs of chemically fixed OME samples taken from the outer commissure but below the first few fibres. B), D) Longitudinal, C), E) transversal cut. Next to the calcite of the fibres (B, C) we see cellular extensions only, while the epithelium portion further proximally (D, E) is abundant in organelles. Ga: Golgi apparatus; ly: lysosome; m: mitochondria; mb: multivesicular body; N: nucleus; rer: rough endoplasmic reticulum.

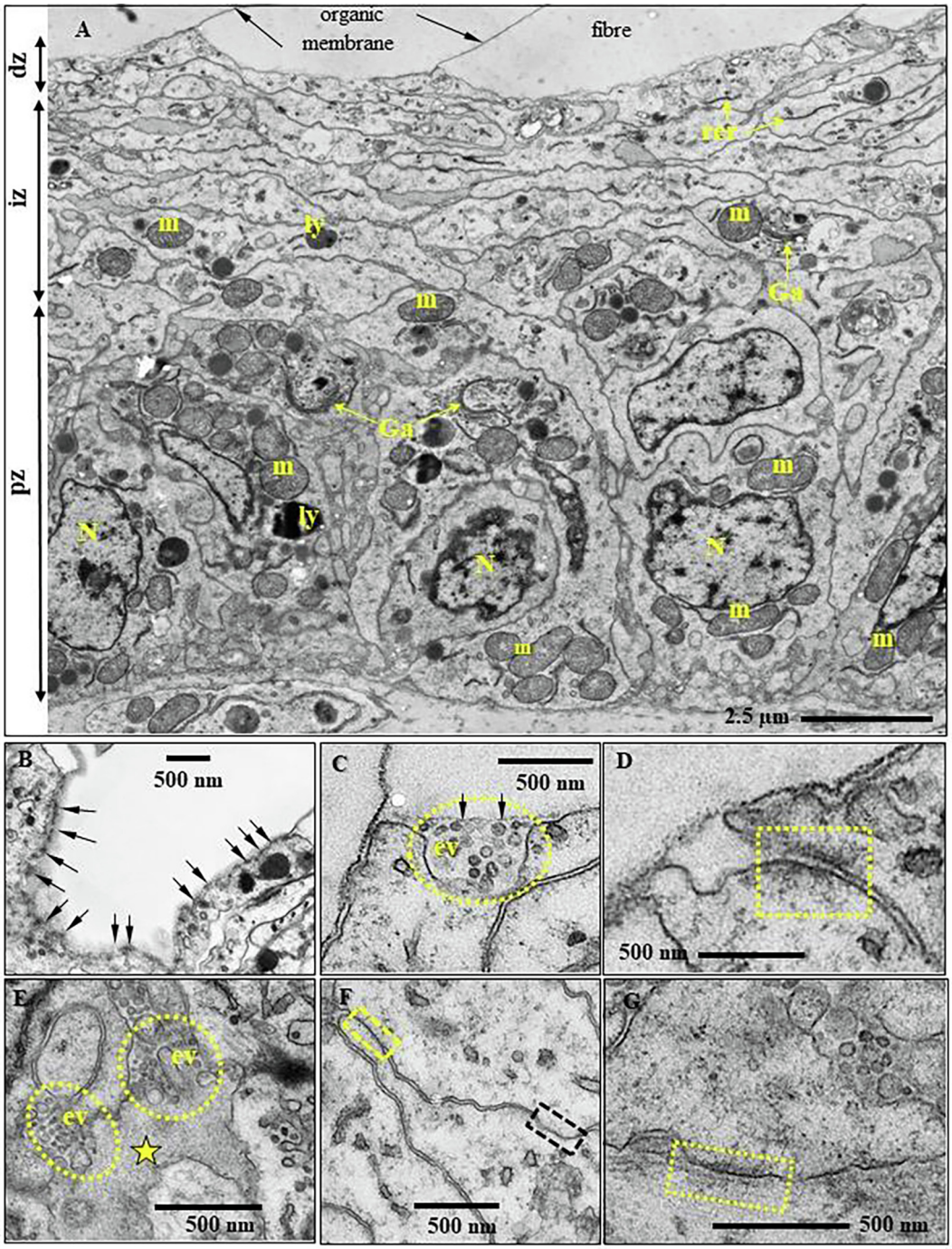

Fig. 7. TEM micrographs of chemically fixed samples taken from the **inner commissure** of *Magellania venosa*. A) The OME is sectioned at an angle to the longitudinal axes of cell extensions. We can distinguish a distal zone (dz), an inner zone (iz) and a proximal zone (pz). Apical cell extensions are elongated and follow the curvature of the fibre. The distal zone consists of numerous small cellular extensions, is devoid of cells with a nucleus and other large organelles. Organelles like mitochondria (m), lysosomes (ly) and Golgy apparatus (Ga) appear in the inner zone; organelle content increases towards the proximal zone at the base of the epithelium; here we find cells with a nucleus (N). B) Oblique cut through a most distal cell extension where apical hemidesmosomes appear as dark plaques (black arrows in B). C) Enlargement showing extracellular vesicles (iv, dashed yellow line) present in the most distal portion of the OME. Regions not attached to the organic membrane have a faint surface coat at their apical side (black arrows in C). D) Enlargement depicting an apical adherence junction resembling an adhesion belt (yellow dashed rectangle). E) Areas with electron dense extracellular material (yellow star) are abundant in distal portions of the OME. These regions contain extracellular vesicles (ev). F) Gap junctions between cells are indicated with black and yellow dashed rectangles. G) Basal hemidesmosomes (yellow dashed rectangle).

present within the apical cell membrane. At the intracellular side the hemidesmosomes bind to tonofilaments (Figs. 8C, D, F, A7), the latter consisting of a bundle of thin filaments (marked with a 't' in Fig. 10D). The tonofilaments bind at the basal side of the cells again to hemidesmosomes. In comparison with the commissure, hemidesmosomes below central shell portions are much thicker. In addition, in high-pressure frozen and freeze-substitution samples we observe that at and near hemidesmosomes OME cells have often two basal plasma membranes (Fig. 10D, E).

At sites where the organic membrane at the proximal, convex

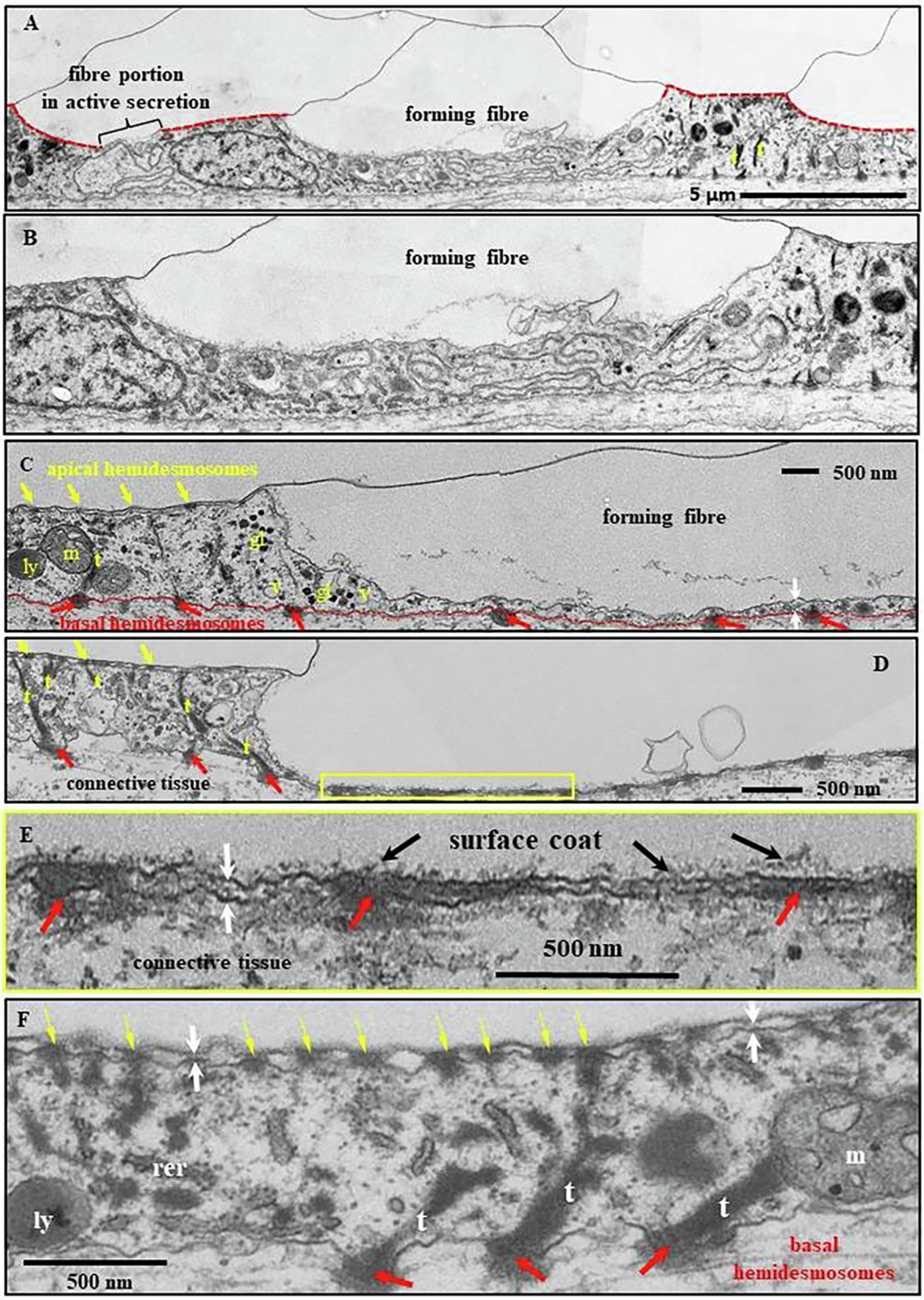

Fig. 8. Aligned arrays of TEM micrographs taken on chemically fixed and decalcified samples obtained from **central shell portions**. Fibres are sectioned transversally. Indicated with a red dotted line are those fibre portions that are not in the state of active secretion. Fibre secretion is finished with the formation of an organic lining along the proximal, convex surface of a fibre. Hence, at sites where the apical cell membrane is attached to the organic membrane lining a fibre portion (red dotted line) OME cells are not producing mineral. The connection between the apical cell membrane and the organic membrane that lines the proximal, convex surface of a fibre occurs via apical hemidesmosomes (yellow arrows in C, D, F). Tonofilaments (C, D, F) within the cells connect apical hemidesmosomes to basal hemidesmosomes (red arrows in C, D, E, F), with the latter being attached to the basal lamina of the OME. Apical hemidesmosomes are small, while basal ones are large (e.g. F). At sites where fibre secretion is active there are neither tonofilaments nor apical hemidesmosomes within cells (A, B, C, D). We observe a thin coat on the surface of cells (black arrows in E). Actively secreting OME cells below fibres from the central shell region are very thin and highly elongated (white arrows in C, E, F).

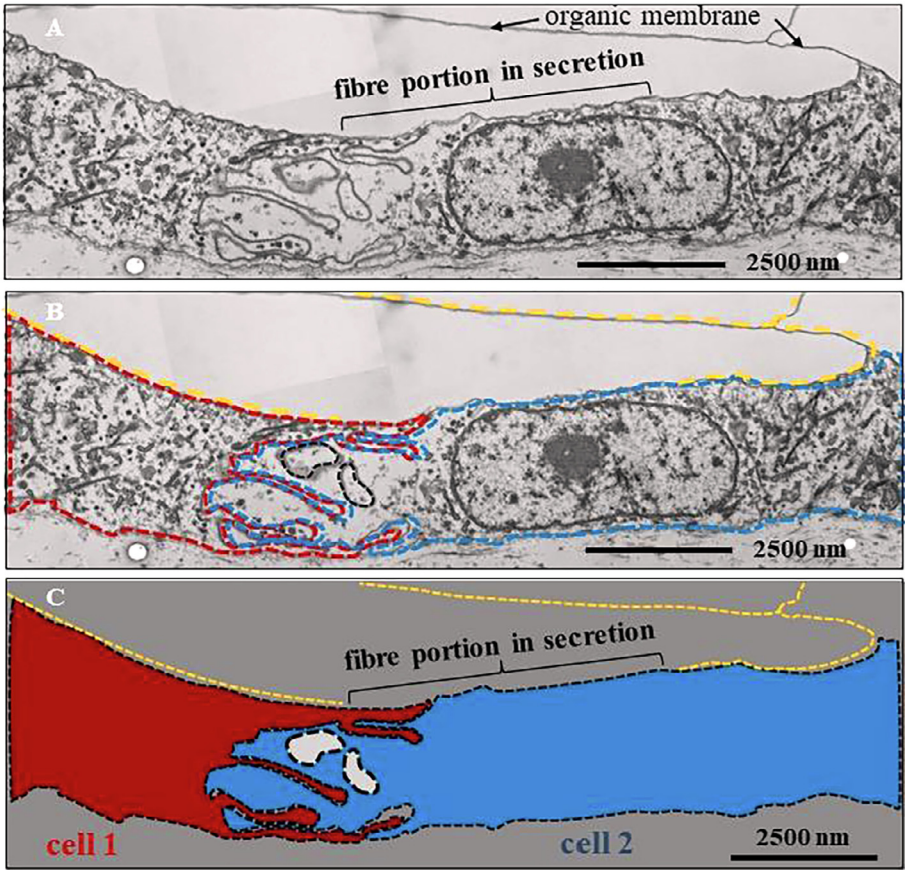

Fig. 9. Topological relation of OME cells to fibres in **central shell portions** of *Magellania venosa*. A, B, C) TEM panorama micrographs of chemically fixed and decalcified samples depicting the ultrastructure of OME cells below transversally sectioned fibres. At sites of ongoing fibre formation the organic membrane along the proximal, convex surface of the fibre is not yet secreted. There is no one-by-one relationship between a fibre and a cell, generally at least two cells contribute to the secretion of the same fibre.

surface of a fibre is absent, OME cells do not contain any hemidesmosomes nor tonofilaments (Figs. 8A, B, C, A7). At these sites calcite secretion is active and material is transported from OME cells to adjacent, newly forming fibres. There is a constant alternation between OME portions that are attached to the organic membrane of fibres and those OME regions where apical cell membranes are detached from fibres (e.g. red dotted line in Fig. 8A). Analysing an epithelial length of 189 μm we find that 14 regions with a total length of 98 μm are attached to the shell via hemidesmosomes and 10 regions, with a total length of 91 μm, are not. Thus, at a given time, about 50% of the OME is not secreting mineral; while the other ~50% of the OME is involved in fibre mineralization (this study and Simonet Roda et al., 2019).

4.5. The mantle epithelium in endopuncta

The shell of *Magellania venosa* contains endopuncta (Figs. 11, A8); these cross the shell from the mantle epithelium to almost the periostracum and, hence, traverse both mineralized shell layers. Between the periostracum and an endopunctum the shell forms a sieve plate containing numerous channels radiating from the lumen of the punctum to the periostracum (Fig. 11A). TEM micrographs of decalcified and chemically fixed samples show that these channels are filled with organic material. The channels are continuous with a hyaline layer present at the distal portion of the punctum, between the sieve plate and numerous microvilli-like cellular extensions of distal punctum cells (Fig. 11B, C). The distal region of the punctum (Fig. 11A, B), the punctum portion that is in the primary layer, is filled with cells rich in lipid droplets, mitochondria, lysosomes and multivesicular bodies. This indicates high metabolic activity in these regions of the punctum. Towards the median region of endopuncta (Fig. 11D), there is a change to a thin, about 1.5 μm thick, single layer of elongated cells; here neighbouring cells overlap with one another (Figs. 11E and A8). Cells within this part of endopuncta contain glycogen, lysosomes, rough endoplasmic reticulum, nuclei and mitochondria; vesicles are rare. At proximal endopuncta regions, the epithelium connects to OME cells (not shown). As the diameter of endopuncta does not decrease with time, cells that line their walls are not secreting mineral. Accordingly, we take morphological characteristics and organelle distribution patterns of OME cells as a reference for comparison with the mineralizing cells encountered at the commissure and the central shell regions.

4.6. Patterns of organelle distribution in OME cells

Results obtained from morphometric analyses are presented in Tables 1 and 2 and Figs. 12 and A9. Tables 1 and 2 provide means and standard deviations for the volume fractions and the volume per 10 μm^2 epithelium, respectively, for mitochondria, organelles of the endo-lysosomes pathway including multivesicular bodies, intracellular vesicles, Golgi apparatus, rough and smooth endoplasmic reticula and glycogen (Fig. A6). Values are given for: (i) the central shell region where the OME is attached to the organic membrane of the fibres, (ii) areas of the central region where the OME is not attached to the organic membrane of fibres and, as an additional control, (iii) the lateral walls of the median regions of the puncta, that do not secrete mineral, (iv) the two central regions pooled together, and (v) the multi-layered inner region of the OME near the commissure. The different stages of the endosomes and lysosomes including multi-vesicular bodies were pooled in the class “endo-lysosomes”. Dark and light vesicles that are not very close to a Golgi apparatus were assigned to the class “intracellular vesicles”. Golgi cisternae and those vesicles that are near the cisternae comprise the class “Golgi apparatus”.

The comparison of the volume fractions of membrane bound organelles in different regions of the outer mantle epithelium (Fig. 12) reveals that the values for the investigated organelles between the two central shell regions (OME attached and OME not attached to the organic membrane of the fibre) are similar, except for the rough

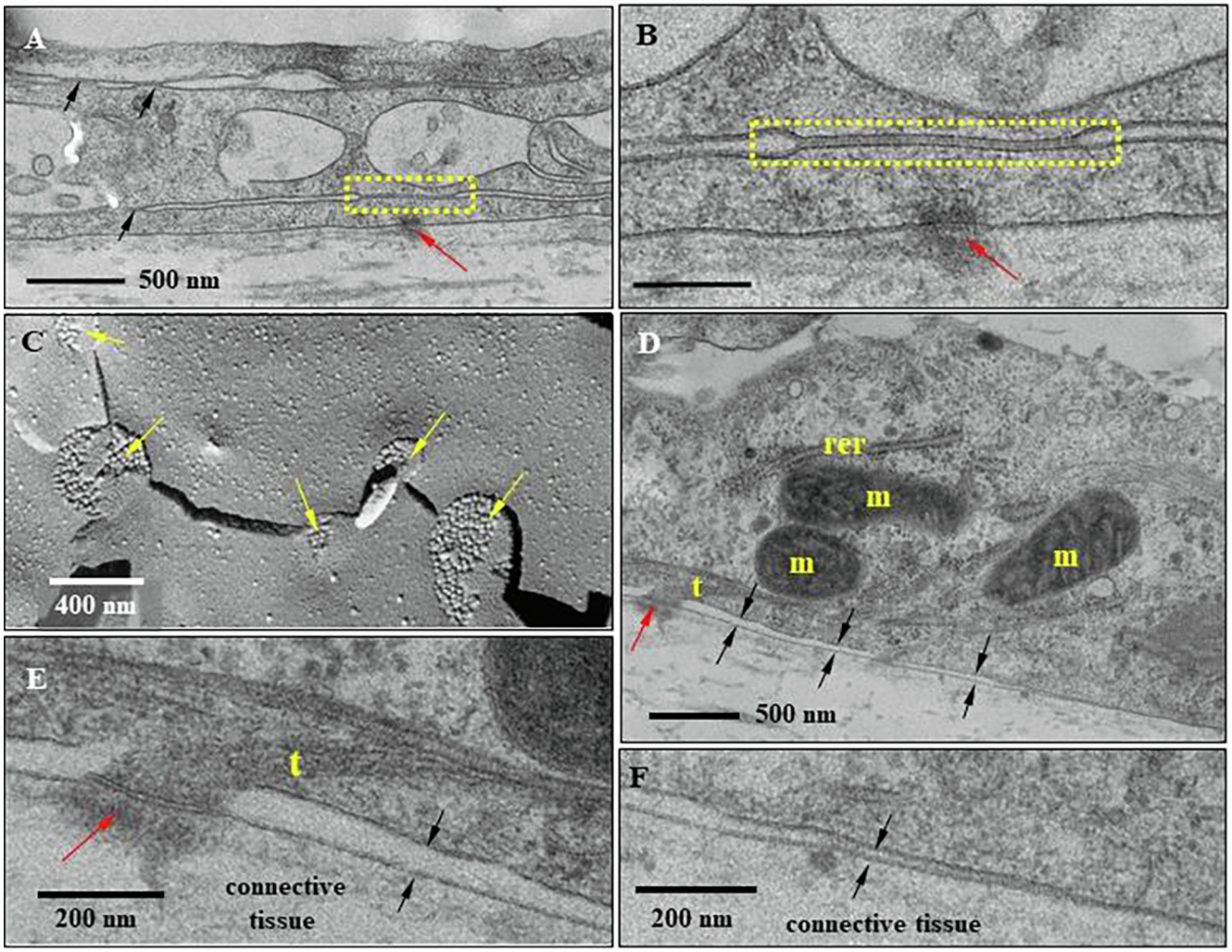

Fig. 10. TEM micrographs recorded from high-pressure frozen OME samples taken from the **central shell region**. The tissue is freeze-substituted (A, B and D–F) or freeze fractured (C). A, B) Many gap junctions can be observed (black arrows and yellow rectangles in A and B). Large hemidesmosomes (red arrows in A, B, D, E) attach the basal membrane of the epithelium to the basal lamina and to tonofilaments (marked with a yellow t in D and E). C) Cryo-SEM image showing 5 gap junctions between two adjoining cells (yellow arrows in C). D) OME cells with two basal membranes (black arrows); rer, rough endoplasmatic reticulum; m, mitochondria.

endoplasmic reticulum. The difference for the latter is statistically significant and is 1.9 times higher in the OME region that is attached to the organic membrane of the fibre. In the lateral walls of puncta, values for the class endo-lysosomes are significantly higher in comparison to values found for the two central shell regions (OME attached and not attached to the organic membrane of the fibre). Volume fractions of mitochondria, endo-lysosomes and intracellular vesicles are significantly higher in the commissure than in the central region, by factors of 2.0 (mitochondria), 2.4 (endo-lysosomes) and 4.7 (intracellular vesicles), respectively.

Since the rate of epithelial mineral transport should be considered across a unit of epithelium area we have normalized the absolute volume of organelles and glycogen to an epithelium area of 10 μm^2 (Fig. A9). In the case of central shell regions the value for rough endoplasmatic reticulum for OME membranes that are attached to the organic membrane of the fibres is significantly higher than where OME membranes are not attached to fibres, as well as for the epithelium of the lateral walls of the puncta. For all organelles shown in Fig. A9 the difference between the commissure and central region is significant; values are always higher in the commissure (Fig. A9). As the distribution of glycogen is concerned, it is abundant in many epithelial cells, except those present at the commissure (Tables 1 and 2). In the central shell section, for OME portions that are not attached to the organic membrane of the fibres, the volume fraction for glycogen is higher than in cells that line the lateral walls of the puncta (Table 1).

The comparison of the mean value of the distal cell membrane area per square µm of epithelium (Fig. 12) between the central shell region (1.3 ± 2 μm^2) (mean ± SD), and the commissure, (1.5 ± 0.5 μm^2), yields no significant difference within standard deviations. However, the proximal cell membrane area (36.5 ± 5.5 μm^2) in the commissure is significantly higher than the membrane area (2.6 ± 1.3 μm^2) in the central shell region. The membrane area of mitochondria per square µm of epithelium of 5.7 ± 1.9 μm^2 in the commissure is significantly higher than the membrane area of 0.5 ± 0.2 μm^2 in the central shell region.

5. Discussion

5.1. Cell proliferation and differentiation

Williams (1968a,b) suggested that in Brachiopoda the generative zone of the mantle epithelium is located at the commissure, at the bottom of the mantle groove. As new cells are permanently produced within the generative zone, Williams postulated the “conveyor belt”

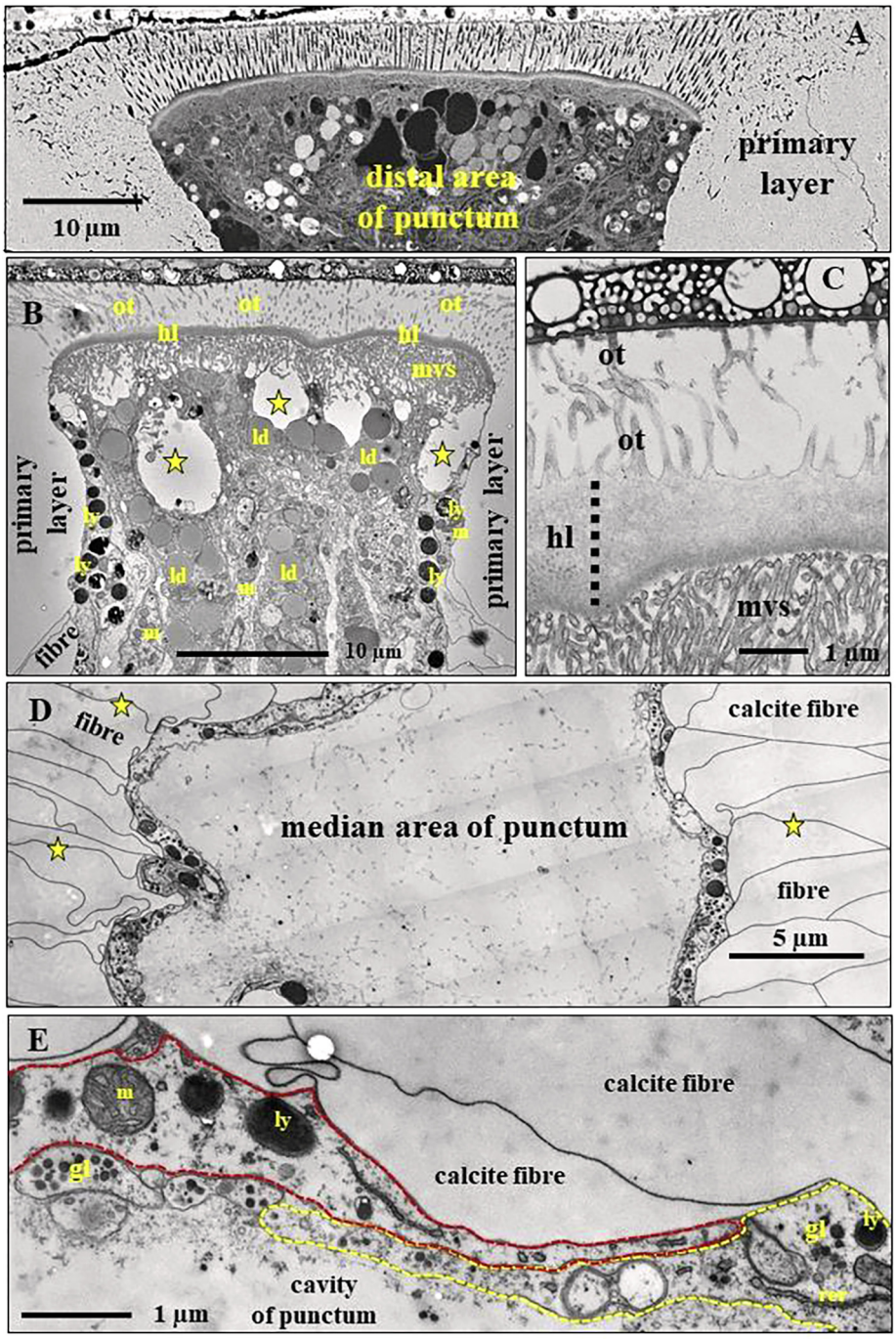

Fig. 11. FE-SEM (A) and TEM (B to E) micrographs of the periostracum, the primary shell layer and an endopunctum in the shell of *Magellania venosa*. A) FE-SEM image of a high-pressure frozen, freeze-substituted but not decalcified shell portion taken on a polished surface showing the primary layer below the periostracum and organic tissue at the uppermost part of a punctum. Above the punctum the shell contains numerous channels radiating from the lumen of the punctum into the periostracum. Apically puncta are completely filled with OME cells. B), C) TEM micrographs of chemically fixed and decalcified samples depicting the uppermost portion of the primary layer above a punctum and the transition to the periostracum. There are channels through the calcite of the primary layer. These are extracellular organic tubes (ot) and are attached to an extracellular hyaline layer (hl) just above microvilli-like cellular extensions (mvs). Within punctum cells, most abundant are lipid droplets (ld), lysosomes (ly) and mitochondria (m). D), E) TEM micrographs of chemically fixed and decalcified sample depicting the median portion of a punctum traversing a stack of fibres. The surface of the punctum is lined by a very thin layer of single, but overlapping cells (E, see also Fig. A8). Most abundant are: lysosomes (ly), mitochondria (m), glycogen (gl), rough endoplasmatic reticulum (rer).

Table 1
Mean values m and their standard deviations σ for the volume fraction of organelles (in %) in the different regions of the outer mantle epithelium. ***n*** is the number of test-fields used for the calculations. "central region all" contains the values of the test-fields of "central region secreting" and "central region attached"; er: endoplasmic reticulum.

organelle volume fraction (V_O)	central region secreting		central region attached		puncta		central region all		commissure	
	m	σ	m	σ	m	σ	m	σ	m	σ
mitochondria	4.0	6.5	4.4	3.9	2.1	2.8	4.2	5.3	8.3	5.3
endo-lysosomes	2.3	2.7	4.5	5.3	12.0	4.0	3.4	4.3	8.2	4.5
vesicles	0.8	0.9	0.4	0.6	1.4	0.9	0.6	0.8	2.8	2.3
Golgi apparatus	0.0	0.0	1.1	2.1	0.0	0.0	0.5	1.6	1	1.4
rough er	3.7	1.6	2	1.8	3.1	1.5	2.9	1.9	2.7	1.2
smooth er	0.7	1.1	0.5	0.8	0.3	0.6	0.6	1	0.4	0.5
glycogen	1.2	1	0.8	0.9	0.3	0.6	1.0	1	0.0	0.0
N	*13*		*12*		*10*		*25*		*13*	

Table 2
Mean values m and their standard deviations σ for the volume of organelles (in μm^3) per 10 μm^2 epithelial area (V_A) in the different regions of the outer mantle epithelium. Values are given with standard deviation. ***n*** is the number of test-fields used for the calculations. "central region all" contains the values of the test-fields of "central region secreting" and "central region attached"; er: endoplasmic reticulum.

organelle volume per 10 μm^2 epithelial area (V_A)	central region secreting		central region attached		puncta		central region all		commissure	
	m	σ	m	σ	m	σ	m	σ	m	σ
mitochondria	0.5	1	0.6	0.7	0.2	0.2	0.6	0.8	8.9	4.9
endo-lysosomes	0.3	0.3	0.8	1.2	1.0	0.6	0.6	0.9	9.4	5.8
vesicles	0.1	0.1	0.1	0.1	0.1	0.1	0.1	0.1	3.4	3.0
Golgi apparatus	0.1	0.1	0.0	0.0	0.0	0.0	0.0	0.1	0.5	1
rough er	0.6	0.4	0.2	0.2	0.2	0.1	0.4	0.4	3	1.1
smooth er	0.1	0.1	0.1	0.1	0.0	0.0	0.1	0.1	0.4	0.6
glycogen	0.2	0.3	0.1	0.1	0.0	0.1	0.1	0.2	0.0	0.0
N	*13*		*12*		*10*		*25*		*13*	

model. This model is based on the notion that, due to permanent cell formation, cells need to move away from the mantle groove and develop anteriorly the OME and posteriorly the IME. As a consequence, OME cells have to undergo a sequence of proliferation events: the secretion of the mucous layer, that of the periostracum and of the mineralized shell layers. However, neither the idea of a proliferation zone located at the base of the mantle groove nor the conveyor belt model is based on firm observations or experiments.

For gastropods and bivalves Kniprath (1975, 1978), using ^{3}H-thymidine labelling, has shown that mitotic cell divisions occur at any site within the OME. The authors did not find an indication of growth centres within the OME. Accordingly, Kniprath concluded that epithelial cells of these molluscs do not change their function and stay in place for secretion of just one structural entity of the shell throughout their lives. In contrast, using a BrdU immunohistochemical method, Fang et al. (2008) observed for the bivalve *Pinctada fucata* that cell divisions were concentrated at a central region of the OME. This indicates, that, depending on the investigated metabolic system, there might be differences in cell proliferation patterns.

For *Magellania venosa* we have not observed any stages of mitosis.

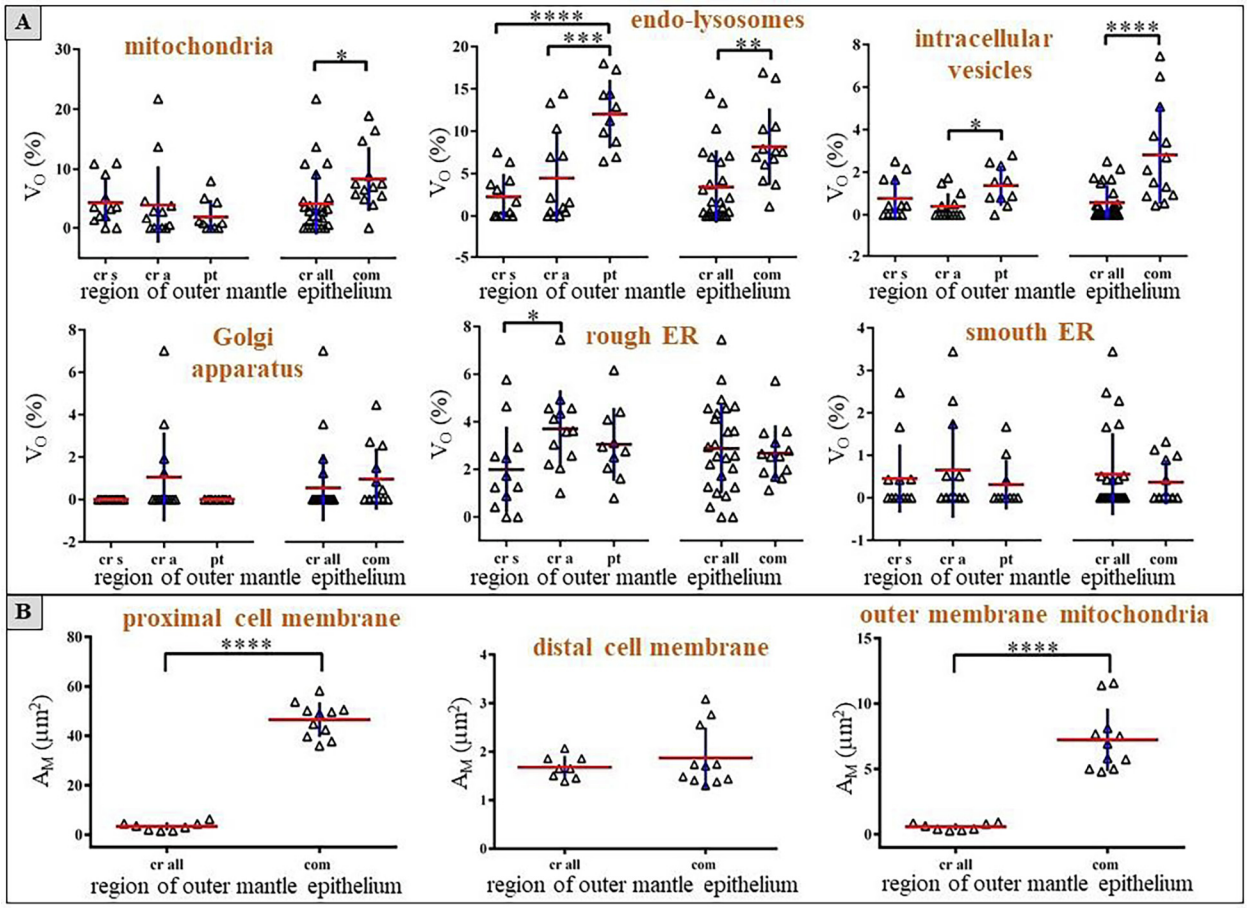

Fig. 12. Volume fraction of membrane-bound organelles. (A) mitochondria, endo-lysosomes, intracellular vesicles, Golgi apparatus, and rough and smooth ER in different regions of the outer mantle epithelium: central shell region that can secrete mineral (cr s), central shell region not involved in secretion (cr a), punctum (pt), secreting and not secreting central shell portions (cr all), commissure (com). (B) Membrane area per 10 μm^2 of the apical and proximal cell membrane and membrane area of the outer membrane of mitochondria for the central shell portion (secreting and not secreting: cr all) and the commissure (com). Results are plotted with the mean (indicated with horizontal red lines in the graphs) and the standard deviation (indicated with vertical lines in the graphs). Stars indicate significant differences of mean values for a given organelle between different outer mantle epithelium regions: *: $P \leq 0.05$; **: $P \leq 0.01$; ***: $P \leq 0.001$; ****: $P \leq 0.0001$.

This points to the fact that mitosis events might be rare in modern terebratulide brachiopods. It is also in agreement with the observed growth rate of 15 − 18 mm per year for juvenile *Magellania venosa* (Baumgarten et al., 2013) which corresponds, when assuming a mean cell length of 10 µm, to about 40–50 cell divisions per day along the median plane of the animal. However, as the mitotic process can be quite fast, observations of these in TEM sections should be rare, and accordingly, sites of cell proliferation in *M. venosa* might so far be undetected. With regard to the conveyor belt mechanism postulated by Williams, it should be noted that in primary shell layer regions of *M. venosa* cell extensions become degraded between the distal ones that secrete the mineral and the proximal ones that secrete the periostracum. This might indicate cell re-differentiation during shell growth and the changing of cell function depending on the type of material they secrete.

According to Williams, regions of the OME at the inner commissure become later part of the mantle epithelium at central shell portions. This implies, that the OME either re-organizes itself from a multi- to a single-layered epithelium or OME cells migrate relative to the calcite fibres towards the shell edge where they differentiate from central-region type cells to commissure type cells. However, the statistically significant higher abundance of organelles of the endo-lysosomal pathway in the commissure in comparison to the abundance of organelles in OME cells at the central shell region and the presence of dense material between cells within the inner commissure strongly argue for a re-organization of OME cells and not for cell migration. Our results indicate that in *Magellania venosa* cell re-organisation takes place between the commissure and the central shell region, where the OME decreases in thickness and successively reduces the number of the long cellular extensions, eventually forming a single cell-layered epithelium devoid of cell extensions.

In both shell regions, the outer commissure and the central shell portion, OME cells connect by hemidesmosomes apically to the organic membranes of the fibres and basally to a thin basal lamina of the OME. At the commissure, apical and basal hemidesmosomes are very small, while they are considerably larger at the central shell portion, particularly the basal hemidesmosomes. This difference can be explained by the presence of large tonofilaments in the mantle epithelium at the central shell portion connecting apical to basal hemidesmosomes. Apparently the tonofilaments together with the hemidesmosomes help to stabilize the position and the shape of epithelial cells that are in direct contact to the fibres. At the commissure tonofilaments cannot occur due to the large number of cellular extensions between the shell and the basal lamina of the OME. Most likely more than one of these large cellular extensions originate from a single cell. Due to its multilayered structure and the large size of the epithelium, additional stabilization of the OME at the commissure appears to be unimportant.

Cryo-preparation of OME cells revealed some additional aspects of OME ultrastructure. High-pressure frozen and freeze-substituted samples of the OME reveal that the tonofilaments are composed of thin fibrils (Fig. 10E). As the tonofilaments are connected to hemidesmosomes, these fibrils represent intermediate filaments that are known to sustain tensile forces particularly well (Kreplak and Fudge, 2007) Another unexpected feature is the presence of two plasma membranes at the basal side of OME cells located close to hemidesmosomes (Fig. 10D–F). This is a new finding for modern brachiopods, to our knowledge, such double cell membranes have up to now been reported only once in the hematophagous insect *Rhodnius prolixu* (Lane and Harrison, 1979).

5.2. Calcite fibre secretion

Simonet Roda et al. (2019) showed that in periodic alternation on the order of 7–9 µm about 50% of the OME is attached to the organic membranes that cover the proximal, convex surface of the calcite fibres. This part of epithelium is in very close contact to the shell, leaving little (i.e. very few nanometers) or no room for an extrapallial space. At these sites, mineral deposition does not take place. It takes place when the cells have detached from the organic membrane that lines the basal surface of the fibres. At these regions, we find that more than one cell is located below the forming fibre Figs. 5 and 9. This observation contradicts claims of Williams (1966, 1968b), who reported that a fibre is formed by one cell only (described for *Notosaria nigricans* and *Hemithiris psittacea*). Secretion of a fibre by more than one cell requires tight cooperation and coordination of neighbouring OME cells as these secrete the mineral and the organic membrane (Simonet Roda et al., 2019). The strong interdigitations of neighbouring cells (Fig. 9) and the very large number of gap junctions between adjacent epithelial cells (Fig. 10A–C) substantiates the need for cell communication and/or exchange of small metabolites.

The tight attachment of apical OME cell membranes to forming fibres raises the question of the dimension of the extrapallial space, the space between the mineral secreting region of the cells and the forming fibre. An answer to this question is important as the width of the extrapallial space affects the mechanism that adds mineral to the growing shell. It is known for molluscs that the extrapallial space between the OME and the shell is only a few tens of nanometers (e.g. about 90 nm in the bivalve *Neotrigonia*, Checa et al., 2014, *Nodipecten nodosus*, Audino et al., 2015). Since mineral may dissolve during sample preparation, we investigated polished samples of resin embedded shells that have been high-pressure frozen and freeze-substituted (this study and Simonet Roda et al., 2019), where both, the mineral and the adjacent outer mantle epithelium are well preserved. These experiments show that that at the growing fibres at sites of mineral deposition the outer mantle epithelium is in direct contact with the calcite fibre, without any extrapallial space in between.

5.3. Mineral transport

Research over the last decades indicated that in shelled organisms hard tissue formation might occur via an amorphous precursor (e.g. Beniash et al., 1997; Beniash et al., 1999; Weiss et al., 2002; Addadi et al., 2003; Weiner et al., 2003; Politi et al., 2004, 2008; Nassif et al., 2005; Nudelman et al., 2008; Jacob et al., 2011; Cartwright et al., 2012; DeVol et al., 2015; Macías-Sánchez et al., 2017; Rousseau, 2018).

In order to test if calcite deposition in *Magellania venosa* fibres takes place via amorphous calcium carbonate (ACC) we performed etching experiments on high-pressure frozen, freeze-substituted and microtome polished surfaces, with shell mineral and the OME being preserved in a native state (Fig. A5). It is known that ACC has a ten times higher solubility than crystalline calcium carbonate and dissolves readily at pH values higher than 7.0 (Brečević and Nielsen, 1989). In previous studies, we have used this characteristic to distinguish between calcite and amorphous Ca-carbonate mineral phases (Seidl and Ziegler, 2012; Seidl et al., 2012). Etching of *Magellania venosa* shell samples at a pH of 9 with the mineral of the shell and the OME being in closest contact to each other showed no mineral dissolution between the forming fibre and the OME (Fig. A5). We find only between fibres a thin layer of mineral that dissolved (compare Fig. A5A with A5bB). We did not find any evidence for the presence of an amorphous precursor at the growing front of fibres. This suggests that the mineral is deposited here directly as calcite rather than via a precursor amorphous phase (ACC). With the applied type of sample preparation crystallization of ACC at preparation can be excluded, since, after shock-freezing the sample remains free of liquid-state water as well as during freeze-substitution, embedding and polishing. This is experimentally verified by our etching experiments, when comparing the micrograph recorded before etching (Fig. A5A) with that after etching at a pH of 9 (Fig. A5B).

Corresponding to our conclusions that we inferred from etching experiments, high-resolution, low-kV EBSD analysis also did not show any ACC between the fibres and the cells of the outer mantle epithelium (Fig. A10). The EBSD signal is a diffraction signal that originates from

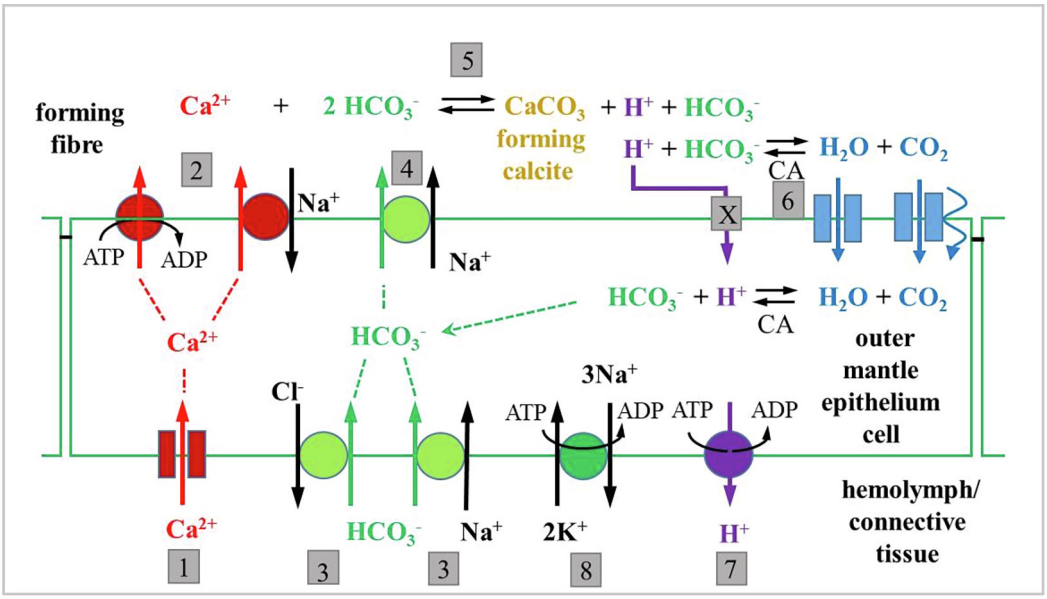

Fig. 13. Major steps of a conceptual model for calcite secretion in the modern brachiopod *Magellania venosa*. (1) Ionized calcium diffuses into the cell through channels along the inwardly directed electrochemical gradient, (2) Ca^{2+} is transported out of the cell, across the apical plasma membrane to the forming fibre, by a Ca^{2+}-transport ATPase or/and a Na^+/Ca^{2+}-exchange mechanism. Carbonate is formed by cell metabolism; but it also enters the cell as HCO_3^- through a (3) HCO_3^-/Cl^- exchange or a HCO_3^-/Na^+ co-transport mechanism. (4) HCO_3 is transported across the apical cell membrane by a HCO_3^-/Na^+ co-transport mechanism or/and a HCO_3^-/Cl^- exchanger (the latter not shown in the model). (5) At the site of mineralization Ca^{2+} reacts with HCO_3^- to form $CaCO_3$ and releasing H^+. (X) To our knowledge there are no proton transporters capable to bring protons from the outside to the inside of the cell against its electrochemical gradient. (6) Carbonic anhydrase catalyses the formation of H_2O and CO_2 from the proton and HCO_3^-; H_2O enters the cell through aquaporin channels and CO_2 diffuses back through the cell membrane into the cytoplasm. In the cytosole the carbonic anhydrase catalyses the reaction back to hydrogencarbonate and a proton. The HCO_3^- is recycled and (8) the proton is transported into the hemolymph by a V-type H^+-ATPase. (8) The inwardly directed sodium gradient is maintained by the $3Na^+/2K^+$ transport-ATPase within the basolateral membrane.

backscattering at lattice planes of crystallized material. Hence, when the electron beam hits lattice planes we obtain a Kikuchi pattern (EBSD signal), while in the case of an amorphous mineral or biopolymers there will be no diffraction at lattice planes and, hence, an EBSD signal will not be formed. We conducted high-resolution EBSD measurements with a step size of about 100 nm (Figs. A10B, A10C) on high-pressure frozen and freeze-substituted *Magellania venosa* fibres that are in direct contact to OME cells (Fig. A10A). We did not find any signs for the presence of an amorphous precursor in any fibres at 100 nm resolution. In contrast, as the EBSD measurement, notably the band contrast, in Fig. A10 shows, the mineral at the growing face of fibres directly next to OME cells is crystallized calcite.

Ultrastructural results of the OME given in this study and the experiments reported by Simonet Roda et al. (2019) allow conclusions about the mechanism of mineral transport from OME cells to the forming fibres. As mentioned in the introduction, transport and deposition of calcium carbonate may occur either via vesicles and exocytosis to the site of mineral deposition (e.g. Aizenberg et al., 1996, Politi et al., 2008, Weiner and Addadi, 2011, Gal et al., 2014) or via ion transport across cell membranes (e.g. Greenaway et al., 1995; Roer, 1980; Wheatly, 1999; Wheatly et al., 2001; Ziegler et al., 2002, 2004) and through the cytoplasm; either with calcium binding proteins or intracellular compartments like the endoplasmic reticulum (e.g.; Ziegler, 2002; Hagedorn and Ziegler, 2002; Hagedorn et al., 2003; Ahearn, 2004; Ziegler et al., 2005). The compart-mentalization is essential as it ensures that high toxic concentrations of ionized calcium in the cytosole are avoided. It was the nanogranular appearance of etch patterns of brachiopod biocalcite in the 50–100 nm size range (Cusack et al., 2008; Schmahl et al., 2008; Simonet Roda et al., 2019), which originally appeared to support the paradigm of biocalcite growth by successive attachment of 50–100 nm nanoparticles. As the fibres of modern *Magellania venosa* are single crystals, the particles – if they exist – need to be ACC which crystallizes homoepitaxially on a substrate crystal. Accordingly, we originally expected to find ACC-filled vesicles of 50–100 nm diameter, which form in the epithelial cells, are exocytosed to attach to the mineral. However, in our high-resolution TEM images there is no positive or direct indication for such a mechanism. Moreover, in the extremely thin epithelial cells of the central shell region (as thin as 20 nm) we did not find organelles or vesicles that would transport solid mineral from cells to the sites of mineralization.

Nevertheless, we observed in OME cells at the commissure small vesicles between the outermost flat cell extensions and the fibrous shell layer. These could be interpreted as exosomes containing mineral and/or organic material that possibly contribute to the formation of the calcite fibres. Contradicting this interpretation is that we do not observe any multivesicular bodies containing exosomes within the OME cells, which are necessary for the secretion of exosomes into extracellular space. Hence, the above mentioned extracellular vesicles are most likely the result of degradation of the long cell extensions, and these are abundant at the commissure. Furthermore, we regard it very unlikely that mechanisms for mineral transport are different between the commissure and the central shell region.

The thin cellular extensions underneath sites of mineral secretion, their direct contact to the forming fibres and the absence of ACC at the growing face of the fibres argue strongly for a vesicle independent mechanism of mineral transport for both, the commissure and the central shell region. Hence, in accord to our findings we propose for modern *Magellania venosa* a transcellular transport of calcium and hydrogen carbonate ions across the OME and the direct formation of calcite at the growing fibre. For the central shell region, this hypothesis is well supported by the extremely thin epithelial cells at sites of mineral secretion. The thinning of these cells diminishes the need of maintaining high calcium gradients within the cytosol and reduces toxic effects on calcium dependent signalling, cytoskeleton stability, and the function of mitochondria. The results of our morphometric analysis support as well transport of ions to sites of shell secretion. OME

cells at the commissure have an about twice as high volume fraction of mitochondria than those within the central shell region, what points to a higher energy consumption of the cells at the commissure. When we compare values of absolute mitochondria volume we find a 15 times higher value for the commissure than for the central region, and for the mitochondrial outer membrane area an 11 times higher value, respectively. This difference is significant. However, it should be kept in mind that additional functions, such as secretion of the periostracum, that of the mucous layer, degradation of cellular extensions and the possibly higher energy costs for higher proliferation rates, evoke as well an increased volume fraction of mitochondria.

Hence, how is then mineral transported to the site of calcification in the modern brachiopod *Magellania venosa*? On the basis of our findings and results reported in literature (Roer, 1980; Roer and Dillaman, 1984; Giraud-Guille, 1984; Cameron and Wood, 1985; Ziegler, 1997; Wheatly, 1999; Wheatly et al., 2001; Hagedorn and Ziegler, 2002; Hagedorn et al., 2003; Ziegler et al., 2004) we developed a conceptual model (Fig. 13) for ionized calcium, carbonate and proton transport for the modern brachiopod *Magellania venosa*. Observations gained in this study that favour a plasma membrane aided ion transport mechanism for shell formation in *Magellania venosa* are: (i) the presence of very thin cell regions at sites of mineral secretion. These thin cells do not require a compartmentation of calcium in the cytoplasm of the cell; (ii) the absence of an amorphous carbonate phase in fibres that are in direct contact with OME cells, hence, fibres that are in active secretion; (iii) the absent or very narrow extrapallial space between the apical membrane of OME cells and the growing fibres, which leaves no space for mineral transport by vesicles; (iv) the lack of evidence for the presence of vesicles transporting ACC.

The major steps of our model are (Fig. 13): (1) Ionized calcium enters the cell passively through calcium channels along the steep inwardly directed electrochemical gradient; (2) From the cytoplasm calcium is transported across the apical cell membrane by a Ca^{2+}-transport ATPase and an Na^+/Ca^{2+}-exchange mechanism. Carbonate ions are formed by cell metabolism or/and (3) enter the cell through a HCO_3^-/Cl^- exchange or a HCO_3^-/Na^+ co-transport mechanism. (4) Hydrogen carbonate is transported by a HCO_3^-/Na^+ co-transporter or/and a HCO_3^-/Cl^- exchanger across the apical cell membrane. (5) At the site of mineralization Ca^{2+} reacts with HCO_3^- to $CaCO_3$ releasing one H^+. To our knowledge there is no transporter which is able to transport protons against its electrochemical gradient from the outside of the cell into the cytoplasm as indicated by the (X) in Fig. 13. However, mineralization can only proceed if the proton is removed into the cytosol to maintain an alkaline pH at the site of mineralization (to reduce the solubility of $CaCO_3$). Numerous studies on a range of different $CaCO_3$ mineralizing organisms have shown the presence of carbonic anhydrases in the mineralized tissue and/or expression of the protein in the mineralizing epithelial cells (e.g. Cameron and Wood, 1985; Miyamoto et al., 1996; Yu et al., 2006; Tambutté et al., 2007; Marie et al., 2008; Moya et al., 2008; Ziegler, 2008) including brachiopods (Isowa et al., 2015). Carbonic anhydrases catalyse the formation of H_2O and CO_2 from H^+ and HCO_3^- as well as the reverse reaction. H_2O can pass back into the cell by aquaporin channels. The passage of the non-polar CO_2 through the membrane is possible by passive diffusion (e.g. Missner et al., 2008), but there are also indications for the existence of CO_2 channels (Endeward et al., 2017). Inside the cell the CO_2 is transformed with water into H^+ and HCO_3^-. The carbonic anhydrase process is indicated as (6) in Fig. 13. (7) The proton is transported from the cytoplasm to the haemolymph by a V-type H^+-ATPase. (8) The inwardly directed sodium gradient is maintained by the $3Na^+/2K^+$ transport-ATPase located in the basolateral cell membrane.

Passage of ionized calcium through specific channels in the cell membrane or/and into intracellular stores plays a major role in cell signalling events and triggers many cell physiological processes (e.g. Grover and Khan, 1992; Simkiss, 1996; Carafoli, 2004; Berridge, 2005; Clapham, 2007). Transcellular calcium ion transport is intrinsic to many epithelial cells. *Non-mineralising epithelial cells* of vertebrate kidney (Kumar, 1995; Moor and Bonny, 2016), the gill and antennal gland epithelium of Crustacea (Flik et al., 1994; Lucu, 1994; Neufeld and Cameron, 1993; Wheatly et al., 2007). Also for *mineralizing epithelial cells*, e.g. those that secrete the mineral in crustacean cuticle (Roer and Dillaman, 1984; Greenaway et al., 1995; Wheatly, 1999; Wheatly et al., 2001; Ziegler et al., 2004), in corals (e.g. Allemand et al., 2004; Böhm et al., 2006; Marshall et al., 2007; Tambutté et al., 2011; Pretet et al., 2013; Fallini et al., 2015; Inoue et al., 2015; Gothmann et al., 2016; Mejía et al., 2018), coccolitophorides (e.g. Gusonne et al., 2006; Langer et al., 2007; McClelland et al., 2017; Hermoso et al., 2017; Yin et al., 2017; Toyofuku et al., 2017; Liu et al., 2018) and foraminifera (e.g. Bentov et al., 2009; De Nooijer et al., 2014; Toyofuku et al., 2017). To our opinion, it is well conceivable that transport of ionized Ca across cell membranes might take place as well at shell mineralization in shell secreting organisms.

6. Conclusions

The shell of modern brachiopods is secreted by the outer mantle epithelium (OME) of the animal. Despite several decades of research, it is still unknown how the mineral is transported from OME cells to the site of mineralization. In order to understand mineral transport and shell secretion, we investigated the ultrastructure of OME cells and their spatial relation to the growing shell. We deduce the following conclusions from our results:

1. The ultrastructure of the OME at the commissure differs significantly from that at central shell regions. The OME at the commissure consists of several cell layers, while at central shell regions it is single-layered.
2. At the commissure, cells form long, lateral extensions towards the shell. These are thin, flat, and in direct contact with the calcite fibres, while proximally they are roundish in cross section.
3. At central shell regions OME cells are considerably thinner in comparison to cells at the commissure. Especially at forming calcite fibres cells are only a few tens of nm thick.
4. Mineral deposition takes only place at sites where the apical membrane of OME cells is in direct contact to the calcite of the fibre. Mineral secretion is terminated with the formation of an organic (likely proteinaceous) membrane which lines the proximal surface of fibres. At these sites, apical hemidesmosomes connect apical cell membranes to the organic lining of the fibres. Tonofilaments connect apical to basal hemidesmosomes. This stabilizes the contact of epithelium and fibres and keeps the mantle in place.
5. Individual fibres are secreted by several cells at the same time. This requires communication and tight cooperation of neighbouring OME cells for the coordinated secretion of organic membrane and mineral, explaining the high abundance of gap junctions between cells.
6. There is not any observation in the cell ultrastructure in our study that can be taken as evidence for a vesicular transport based mineralization process. On the contrary, the absent or very narrow (in the range of nanometers) space between the epithelium and the growing fibres, together with the absence of significant differences in the volume fraction of vesicles between secreting and non-secreting regions of the OME, as well as the extreme reduction in cell thickness at sites of mineral secretion suggests, that in modern *Magellania venosa* (and likely in all Rhynchonellida and Terebratulida forming the fibrous microstructure) mineral transport to the sites of mineralization occurs via ion transport mechanisms through the cell membrane and not by transport of mineral by organelles such as vesicles.

Acknowledgments

We thank two anonymus referees for their thoughtful reviews and helpful comments. Very many thanks to Florian Böhm for reading and discussing the manuscript. We thank Renate Kunz of the Central Facility for Electron Microscopy of Ulm University for technical support and assistance. This is a BASE-LINE Earth project with the funding of the European Union's Horizon 2020 research and innovation program under grant agreement No. 643084. In part this work was supported by the Deutsche Forschungsgemeinschaft (Zi 368/11-1).

Author's contribution

MSR and AZ performed all EM analytical work: biochemical preparation, FE-SEM, TEM, imaging and morphometry data analysis. UR helped with TEM imaging and evaluation of morphometric data sets. AZ, EG, MSR wrote the manuscript. WS, AE, XY, MG contributed to the final version of the manuscript. VH, JL, DH took care of sampling, transport and culturing of live *Magellania venosa*.

Appendix A. Supplementary data

Supplementary data to this article can be found online at https://doi.org/10.1016/j.jsb.2019.05.002.

References

Addadi, L., Raz, S., Weiner, S., 2003. Taking advantage of disorder: amorphous calcium carbonate and its roles in biomineralization. Adv. Mater. 15, 959–970.

Ahearn, G.A., Mandal, P.K., Mandal, A., 2004. Calcium regulation in crustaceans during the molt cycle: a review and update. Comp. Biochem. Physiol. 247–257.

Aizenberg, B.J., Lambert, G., Addadi, L., Weiner, S., 1996. Stabilization of amorphous calcium carbonate by specialized macromolecules in biological and synthetic precipitates. Adv. Mater. 8, 222–226.

Allemand, D., Ferrier-pagès, C., Furla, P., Houlbrèque, F., Darwin, C., 2004. Biomineralisation in reef-building corals: from molecular mechanisms to environmental control. C. R. Palevol. 3, 453–467.

Angiolini, L., Jadoul, F., Leng, M.J., Stephenson, M.H., Rushton, J., Chenery, S., Crippa, G., 2009. How cold were the Early Permian glacial tropics? testing sea-surface temperature using the oxygen isotope composition of rigorously screened brachiopod shells. J. Geol. Soc. London 166, 933–945.

Auclair, A.C., Joachimski, M.M., Lécuyer, C., 2003. Deciphering kinetic, metabolic, and environmental controls on stable isotope fractionations between seawater and the shell of *Terebratalia transversa* (Brachiopoda). Chem. Geol. 202, 59–78.

Audino, J.A., Marian, J.E.A.R., Wanninger, A., Lopes, S.G.B.C., 2015. Mantle margin morphogenesis in *Nodipecten nodosus* (Mollusca, Bivalvia): new insights into the development and the roles of bivalve pallial folds. BMC Dev. Biol. 15, 1–22.

Bates, N.R., Brand, U., 1991. Environmental and physiological influences on isotopic and elemental compositions of brachiopod shell calcite: implications for the isotopic evolution of Paleozoic oceans. Chem. Geol. 94, 67–78.

Baumgarten, S., Laudien, J., Jantzen, C., Haussermann, V., Försterra, G., 2013. Population structur, growth and production of a recent brachiopod from the Chilean fjord region. Mar. Ecol. 35, 401–413. https://doi.org/10.1111/maec.12097.

Berridge, M.J., 2005. Unlocking the secrets of cell signaling. Annu. Rev. Physiol. 67, 1–21.

Beniash, E., Aizenberg, J., Addadi, L., Weiner, S., 1997. Amorphous calcium carbonate transforms into calcite during sea urchin larval spicule growth. Proc. R. Soc. Lond. B 264, 461–465.

Beniash, E., Addadi, L., Weiner, S., 1999. Cellular control over spicule formation in sea urchin embryos a structural approach. J. Struct. Biol. 125, 50–62.

Bentov, S., Brownlee, C., Erez, J., 2009. The role of seawater endocytosis in the biomineralization process in calcareous foraminifera. PNAS 106, 21500–21504.

Bonifacino, J.S., Glick, B.S., 2004. The mechanism of vesicle budding and fusion. Cell 116, 153–166.

Böhn, F., Gussone, N., Eisenhauer, A., Dullo, W.C., Reynaud, S., Paytan, A., 2006. Calcium isotope fractionation in modern scleractinian corals. Geochim. Cosmochim. Acta 70, 4452–4462.

Brand, U., Logan, A., Bitner, M., Griesshaber, E., Azmy, K., Buhl, D., 2011. What is the ideal proxy of Paleozoic seawater chemistry? Mem. Assoc. Australas. Palaeontol. 41, 9–24.

Brečević, L., Nielsen, A.E., 1989. Solubility of amorphous calcium carbonate. J. Cryst. Growth 98, 504–510.

Carafoli, E., 2004. Special issue: calium signalling and desease. Biochem. Biophys. Res. Commun. 322, 1097.

Carlson, S.J., 2016. The evolution of brachiopoda. Annu. Rev. Earth Planet. Sci. 409–38. https://doi.org/10.1146/annurev-earth-060115-012348.

Carpenter, S.J., Lohmann, K.C., 1995. $\delta^{18}O$ and $\delta^{13}C$ values of modern brachiopod shells. Geochim. Cosmochim. Acta 59, 3749–3764.

Casella, L.A., Griesshaber, E., Simonet Roda, M., Ziegler, A., Mavromatis, V., Henkel, D., Laudien, J., Häussermann, V., Neuser, R.D., Angiolini, L., Dietzel, M., Eisenhauer, A., Immenhauser, A., Brand, U., Schmahl, W.W., 2018a. Micro- and nanostructures reflect the degree of diagenetic alteration in modern and fossil brachiopod shell calcite: A multi-analytical screening (CL, Fe-SEM, AFM, EBSD). Palaeogeogr. Palaeoclimatol. Palaeoecol. 502, 13–30.

Casella, L.A., Simonet Roda, M., Angiolini, L., Ziegler, A., Schmahl, W.W., Brand, U., Griesshaber, E., 2018b. Archival biogenic micro- and nanostructure data analysis: signatures of diagenetic systems Data in Brief Archival biogenic micro- and nanostructure data analysis: signatures of diagenetic systems. Data Brief 19, 299–311.

Casella, L.A., He, S., Griesshaber, E., Fernández-Díaz, L., Greiner, M., Harper, E.M., Jackson, D., Ziegler, A., Mavromatis, V., Dietzel, M., Eisenhauer, A., Immenhauser, Veintemillas-Verdaguer, S., Brand, U., Schmahl, W.W., 2018c. Hydrothermal alteration of aragonitic biocarbonates: assessment of micro- and nanostructural dissolution-reprecipitation and constraints of diagenetic overprint from quantitative statistical grain-area analysis. Biogeosciences 15, 7451–7484.

Cartwright, J., Checa, A., Gale, D.J., Gebauer, D., Sainz-Díaz, C., 2012. Calcium carbonate polyamorphism and its role in biomineralization: how many amorphous calcium carbonates are there? Angew. Chem. Int. Ed. Engl. 51. https://doi.org/10.1002/anie.201203125.

Cameron, J.N., Wood, C.M., 1985. Apparent H^+ excretion and CO_2 dynamics accompanying carapace mineralization in the blue crab (*Callinectes sapidus*) following moulting. J. Exp. Biol. 114, 181–196.

Checa, A.G., Salas, C., Harper, E.M., Bueno-pe, J.D.D., 2014. Early stage biomineralization in the periostracum of the "living fossil" *Bivalve Neotrigonia*. PLoS One 9. https://doi.org/10.1371/journal.pone.0090033.

Clapham, D.E., 2007. Calcium signalling. Cell 131, 1047–1058.

Cross, E.L., Harper, E.M., Peck, L.S., 2018. A 120-year record of resilience to environmental change in brachiopods. Glob. Chang. Biol. 24, 2262–2271.

Cusack, M., 2001. Biomineralization in brachiopod shells. Paleontol. Soc. Pap. 7, 105–116.

Cusack, M., Dauphin, Y., Chung, P., Pérez-Huerta, A., Cuif, J.P., 2008. Multiscale structure of calcite fibres of the shell of the brachiopod *Terebratulina retusa*. J. Struct. Biol. 164, 96–100.

De Nooijer, L.J., Spero, H.J., Erez, J., Bijma, J., Reichart, G.J., 2014. Biomineralization in perforate foraminifera. Earth Sci. Rev. 135, 48–58.

DeVol, R.T., Sun, C.-Y., Marcus, M.A., Coppersmith, S.N., Myneni, S.C.B., Gilbert, P.U.P.A., 2015. Nanoscale transforming mineral phases in fresh nacre. J. Am. Chem. Soc. 137, 13325–13333.

Endeward, V., Arias-Hidalgo, M., Al-Samir, S., Gros, G., 2017. CO_2 permeability of biological membranes and role of CO_2 channels. Membranes 7, 61.

Fabritius, H., Ziegler, A., 2003. Analysis of Ca CO_3 deposit formation and degradation during the molt cycle of the terrestrial isopod *Porcellio scaber* (Crustacea, Isopoda). J. Struct. Biol. 142, 281–291.

Fabritius, H., Walther, P., Ziegler, A., 2005. Architecture of the organic matrix in the sternal CaCO3 deposits of *Porcellio scaber* (Crustacea, Isopoda). J. Struct. Biol. 150, 190–199.

Fallini, G., Fermani, S., Goffredo, S., 2015. Seminars in Cell & Developmental Biology Coral biomineralization: a focus on intra-skeletal organic matrix and calcification. Semin. Cell Dev. Biol. 46, 17–26.

Fang, Z., Feng, Q., Chi, Y., Xie, L., Zhang, R., 2008. Investigation of cell proliferation and differentiation in the mantle of *Pinctada fucata* (Bivalve, Mollusca). Mar. Biol. 153, 745–754.

Flik, G., Verbost, P.M., Atsma, W., 1994. Calcium transport in gill plasma membranes of the crab *Carcinus maenas*: evidence for carriers driven by ATP and A Na^+ gradient. J. Exp. Biol. 195, 109–122.

Gal, A., Kahil, K., Vidavsky, N., De Vol, R.T., Gilbert, P.U.P.A., Fratzl, P., Weiner, S., Addadi, L., 2014. Particle accretion mechanism underlies biological crystal growth from an amorphous precursor phase. Adv. Funct. Mater. 24, 5420–5426.

Garbelli, C., 2017. Shell microstructures in lopingian brachiopods: implications for fabric evolution and calcification Riv. Ital. Paleontol. Stratigr. 123, 541–560.

Gaspard, D., Nouet, J., 2016. Hierarchical architecture of the inner layers of selected extant rhynchonelliform brachiopods. J. Struct. Biol. 196, 197–205.

Giddins, T.H., 2003. Freeze-substitution protocols for improved visualization of membranes in high-pressure frozen samples. J. Microsc. 212, 53–61.

Giraud-Guille, M.-M., 1984. Calcification initiation sites in the crab cuticle: the interprismatic septa. Cell Tissue Res. 236, 413–420.

Goetz, A.J., Griesshaber, E., Neuser, R.D., Ter, C.L., Hner, M.H., Harper, E., Schmahl, W.W., 2009. Calcite morphology, texture and hardness in the distinct layers of rhynchonelliform brachiopod shells. Eur. J. Mineral. 21, 303–315.

Goetz, A.J., Steinmetz, D.R., Griesshaber, E., Zaefferer, S., Raabe, D., Kelm, K., Irsen, S., Sehrbrock, A., Schmahl, W.W., 2011. Interdigitating biocalcite dendrites form a 3-D jigsaw structure in brachiopod shells. Acta Biomater. 7, 2237–2243.

Gothmann, A.M., Bender, M.L., Blättler, C.L., Swart, P.K., Giri, S.J., Adkins, J.F., Stolarski, J., Higgins, J.A., 2016. Calcium isotopes in scleractinian fossil corals since the Mesozoic: implications for vital effects and biomineralization through time. Earth Planet. Sci. Lett. 444, 205–214.

Grover, A.K., Khan, I., 1992. Calcium pump isoforms: diversity, selectivity and plasticity. Cell Calcium 13, 9–17.

Greenaway, P., Dillaman, R.M., Roer, R.D., 1995. Quercitin-dependent ATPase activity in the hypodermal tissue of *Callinectes sapidus*, during the moult cycle. Comp. Biochem. Physiol. 111A, 303–312.

Griesshaber, E., Schmahl, W.W., Neuser, R., Pettke, T., Blüm, M., Mutterlose, J., Brand, U., 2007. Crystallographic texture and microstructure of terebratulide brachiopod shell calcite: an optimized materials design with hierarchical architecture. Am. Mineral. 92, 722–734.

Griesshaber, E.R., Kelm, K.L., Sehrbrock, A.N., Mader, W.E., 2009. Amorphous calcium carbonate in the shell material of the brachiopod *Megerlia truncata*. Eur. J. Mineral. 21, 715–723.
Griesshaber, E., Schmahl, W.W., Ubhi, H.S., Huber, J., Nindiyasari, F., Maier, B., Ziegler, A., 2013. Homoepitaxial meso- and microscale crystal co-orientation and organic matrix network structure in *Mytilus edulis* nacre and calcite. Acta Biomater. 9, 9492–9502.
Griesshaber, E., Yin, X., Ziegler, A., Kelm, K., Checa, A., Eisenhauer, A., Schmahl, W.W., 2017. Patterns of mineral organization in carbonate biological hard materials. In: Heuss-Assbichler, S., Amthauer, G., John, M. (Eds.), Highlights in Applied Mineralogy. De Gruyter, pp. 245–272.
Grossman, E.L., Mii, H.-S., Zhang, C., Yancey, T.E., 1996. Chemical variation in Pennsylvanian brachiopod shells-diagenetic, taxonomic, microstructural, and seasonal effects. J. Sediment. Res. 66, 1011–1022.
Gussone, N., Langer, G., Eisenhauer, A., 2006. Cellular calcium pathways and isotope fractionation in *Emiliania huxleyi*. Geology 34, 625–628.
Hagedorn, M., Ziegler, A., 2002. Analysis of Ca^{2+} uptake into the smooth endoplasmic reticulum of permeabilised sternal epithelial cells during the moulting cycle of the terrestrial isopod *Porcellio scaber*. J. Exp. Biol. 205, 1935–1942.
Hagedorn, M., Weihrauch, D., Towle, D.W., Ziegler, A., 2003. Molecular characterisation of the smooth endoplasmic reticulum Ca^{2+}-ATPase of *Porcellio scaber* and its expression in sternal epithelia during the moult cycle. J. Exp. Biol. 206, 2167–2175.
Hermoso, M., Lefeuvre, B., Minoletti, F., de Rafélis, M., 2017. Extreme strontium concentrations reveal specific biomineralization pathways in certain coccolithophores with implications for the Sr/Ca paleoproductivity proxy. PLoS One 12. https://doi.org/10.1371/journal.pone.0185655.
Inoue, M., Gussone, N., Koga, Y., Iwase, A., Suzuki, A., Sakai, K., Kawahata, H., 2015. Controlling factors of Ca isotope fractionation in scleractinian corals evaluated by temperature, pH and light controlled culture experiments. Geochim. Cosmochim. Acta 167, 80–92.
Isowa, Y., Sarashina, I., Oshima, K., Kito, K., Hattori, M., Endo, K., 2015. Proteome analysis of shell matrix proteins in the brachiopod *Laqueus rubellus*. Proteome Sci. 13, 21.
Jacob, D.E., Wirth, R., Soldati, A.L., Wehrmeister, U., Schreiber, A., 2011. Amorphous calcium carbonate in the shells of adult Unionoida. J. Struct. Biol. 173, 241–249.
Karnovsky, M., 1965. A formaldehyde-glutaraldehyde fixative of high quality for use in electron microscopy. J. Cell Biol. 27, 137–138.
Kniprath, E., 1978. Growth of the shell-field in mytilus (Bivalvia). Zool. Scripta. 7, 119–120.
Kniprath, E., 1975. Das wachstum des mantels von *Lymnaea stagnalis* (Gastropoda). Cytobiologie 10, 260–267.
Kreplak, L., Fudge, D., 2007. Biomechanical properties of intermediate filaments: from tissues to single filaments and back. BioEssays 29, 26–35.
Kumar, R., 1995. Calcium transport in epithelial cells of the intestine and kidney. J. Cell. Biochem. 57, 392–398.
Lane, N.J., Harrison, J.B., 1979. An unusual cell surface modification: a double plasma membrane. J. Cell Sci. 39, 355–372.
Langer, G., Gussone, N., Kiel, D., Eisenhauer, A., 2007. Calcium isotope fractionation during coccolith formation in *Emiliania huxleyi*: independence of growth and calcification rate. Geochem. Geophys. Geosyst. 8, Q05007.
Lee, D.E., Robinson, J.H., Witman, J.D., Copeland, S.E., Harper, E.M., Smith, F., Lamare, M., 2011. Observations on recruitment, growth and ecology in a diverse living brachiopod community, doubtful Sound, Fiordland, New Zealand. Spec. Pap. Palaeontol. 84, 177–191.
Liu, Y.-W., Eagle, R.A., Aciego, S.M., Gilmore, R.E., Ries, J.B., 2018. A coastal coccolithophore maintains pH homeostasis and switches carbon sources in response to ocean acidification. Nat. Commun. 9, 2857.
Lowenstam, H.A., 1961. Mineralogy, O^{18}/O^{16} ratios, and Strontium and Magnesium contents of recent and fossils brachiopods and their bearing on the history of the oceans. J. Geol. 69, 241–260.
Lucu, C., 1994. Calcium transport across isolated gill epithelium of carcinus. J. Exp. Zool. 268, 339–346.
Macías-Sánchez, E., Willinger, M.G., Pina, C.M., Checa, A.G., 2017. Transformation of ACC into aragonite and the origin of the nanogranular structure of nacre. Sci. Rep. https://doi.org/10.1038/s41598-017-12673-0.
Marie, B., Luquet, G., Bédouet, L., Milet, C., Guichard, N., Medakovic, D., Marin, F., 2008. Nacre calcification in the freshwater mussel *Unio pictorum*: carbonic anhydrase activity and purification of a 95 kDa calcium-binding glycoprotein. ChemBioChem 9, 2515–2523.
Marshall, A.T., Clode, P.L., Russell, R., Prince, K., Stern, R., 2007. Electron and ion microprobe analysis of calcium distribution and transport in coral tissues. J. Exp. Biol. 210, 2453–2463.
McClelland, H.L.O., Bruggeman, J., Hermoso, M., Rickaby, R.E.M., 2017. The origin of carbon isotope vital effects in coccolith calcite. Nat. Commun. 8, 14511.
Mejía, M., Paytan, A., Eisenhauer, A., Böhm, F., Kolevica, A., Bolton, C., Méndez-Vicente, A., Abrevaya, L., Isensee, K., 2018. Controls over δ44/40Ca and Sr/Ca variations in coccoliths: new perspectives from laboratory cultures and cellular models. Earth Plan. Sci. Let. 481, 48–60.
Merkel, C., Griesshaber, E., Kelm, K., Neuser, R., Jordan, G., Logan, A., Mader, W., Schmahl, W.W., 2007. Micromechanical properties and structural characterization of modern inarticulated brachiopod shells. J. Geophys. Res. 112, G02008.
Merz, W.A., 1967. Die streckenmessung an gerichteten strukturen im mikroskop und ihre anwendung zur bestimmung von oberflächen-volumen-relationen im knochengewebe. Mikroskopie 22, 132–142.
Missner, A., Kügler, P., Saparov, S.M., Sommer, K., Mathai, J.C., Zeidel, M.L., Pohl, P., 2008. Carbon dioxide transport through membranes. J. Biol. Chem. 283, 25340–25347.
Miyamoto, H., Miyashita, T., Okushima, M., Nakano, S., Morita, T., Matsushiro, A., 1996. A carbonic anhydrase from the nacreous layer in oyster pearls. Proc. Nat. Acad. Sci. 93, 9657–9660.
Moor, M.B., Bonny, O., 2016. Ways of calcium reabsorption in the kidney. Am. J. Physiol. Renal Physiol. 310, 1337–1350.
Moya, A., Tambutté, S., Bertucci, A., Tambutté, E., Lotto, S., Vullo, D., Supuran, C.T., Allemand, D., Zoccola, D., 2008. Carbonic anhydrase in the scleractinian coral *Stylophora pistillata* characterization, localization, and role in biomineralization. J. Biol. Chem. 283, 25475–25484.
Nassif, N., Pinna, N., Gehrke, N., Antonietti, M., Jäger, C., Cölfen, H., 2005. Amorphous layer around aragonite platelets in nacre. PNAS 102, 12653–12655.
Neufeld, D.S., Cameron, J.N., 1993. Transepithelial movement of calcium in crustaceans. J. Exp. Biol. 184, 1–16.
Nindiyasari, F., Ziegler, A., Griesshaber, E., Fernández-Díaz, L., Huber, J., Walther, P., Schmahl, W.W., 2015. Effect of hydrogel matrices on calcite crystal growth morphology, aggregate formation, and co-orientation in biomimetic experiments and biomineralization environments. Cryst. Growth Des. 15, 2667–2685.
Nudelman, F., Shimoni, E., Klein, E., Rousseau, M., Bourrat, X., Lopez, E., Addadi, L., Weiner, S., 2008. Forming nacreous layer of the shells of the bivalves *Atrina rigida* and *Pinctada margaritifera*. J. Struct. Biol. 162, 290–300.
Parkinson, D., Curry, G.B., Cusack, M., Fallick, A.E., 2005. Shell structure, patterns and trends of oxygen and carbon stable isotopes in modern brachiopod shells. Chem. Geol. 219, 193–235.
Peck, L.S., Brockington, S., Brey, T., Trans, P., Lond, R.S., Peck, L.S., Brockington, S., Brey, T., 1997. Growth and metabolism in the Antarctic brachiopod *Liothyrella uva*. Philos. Trans. R. Soc. London Biol. Sci. 352, 851–858.
Peck, L., 2007. Brachiopods and climate change Brachiopods and climate change. Earth Environ. Sci. Trans. R. Soc. Edinburgh 98, 451–456.
Politi, Y., Metzler, R.A., Abrecht, M., Gilbert, B., Wilt, F.H., Sagi, I., Addadi, L., Weiner, S., Gilbert, P.U.P.A., 2008. Transformation mechanism of amorphous calcium carbonate into calcite in the sea urchin larval spicule. PNAS 105, 17362–17366.
Politi, Y., Arad, T., Klein, E., Weiner, S., Addadi, L., 2004. Sea urchin spine calcite forms via a transient amorphous calcium carbonate phase. Science 306, 1161–1164.
Pretet, C., Samankassou, E., Felis, T., Reynaud, S., Böhm, F., Eisenhauer, A., Ferrier-pagès, C., Gattuso, J., Camoin, G., 2013. Constraining calcium isotope fractionation (δ 44/40 Ca) in modern and fossil scleractinian coral skeleton. Chem. Geol. 340, 49–58.
Roark, A., Grossman, E.L., Lebold, J., 2015. Low seasonality in central equatorial Pangea during a late Carboniferous high stand based on high-resolution isotopic records of brachiopod shells. Geol. Soc. Am. Bull. 128, 597–608.
Roduit, N., 2008. JMicroVision: Image analysis toolbox for measuring and quantifying components of high-definition images. Version 1.2.7.
Roer, R.D., 1980. Mechanisms of resorption and deposition of calcium in the carapace of the crab *Carcinus maenas*. J. Exp. Biol. 88, 205–218.
Roer, R., Dillaman, R., 1984. The structure and calcification of the crustacean cuticle. Amer. Zool. 24, 893–909.
Rosenberg, G.D., Hughes, W.W., Tkachuck, R.D., 1988. Intermediary metabolism and shell growth in the brachiopod *Terebratalia transversa*. Lethaia 21, 219–230.
Rothman, J.E., Wieland, F.T., 1996. Protein sorting by transport vesicles. Science 272, 227–234.
Rousseau, M., 2018. Nacre: a biomineral, a natural biomaterial, and a source of bio-inspiration. In: Heuss-Assbichler, S., Amthauer, G., John, M. (Eds.), Highlights in Applied Mineralogy. De Gruyter, pp. 285–300.
Samtleben, C., Munnecke, A., Bickert, T., 2001. Shell succession, assemblage and species dependent effects on the C r O-isotopic composition of brachiopods — examples from the Silurian of Gotland. Chem. Geol. 175, 61–107.
Schmahl, W.W., Griesshaber, E., Neuser, R., Lenze, A., Job, R., Brand, U., 2004. The microstructure of the fibrous layer of terebratulide brachiopod shell calcite. Eur. J. Mineral. 16, 693–697.
Schmahl, W.W., Griesshaber, E., Merkel, C., Kelm, K., Deuschle, J., Neuser, R.D., Goetz, A.J., Sehrbrock, A., Mader, W., 2008. Hierarchical fibre composite structure and micromechanical properties of phosphatic and calcitic brachiopod shell biomaterials – an overview. Mineral. Mag. 72, 541–562.
Schmahl, Wolfgang Wilhelm, Griesshaber, E., Kelm, K., Ball, A., Goetz, A., Xu, D., Kreitmeier, L., Guntram, J., 2012. Towards systematics of calcite biocrystals: insight from the inside. Z. Krist. 227, 604–611.
Seidl, B.H.M., Ziegler, A., 2012. Electron microscopic and preparative methods for the analysis of isopod cuticle. Zookeys 176, 73–85.
Seidl, B.H.M., Reisecker, C., Hild, S., Griesshaber, E., Ziegler, A., 2012. Calcite distribution and orientation in the tergite exocuticle of the isopods *Porcellio scaber* and *Armadillidium vulgare* (Oniscidea, Crustacea) – a combined FE-SEM, polarized SCμ-RSI and EBSD study. Z. Krist. 227, 777–792.
Simkiss, K., 1996. Calcium transport across calcium-regulated cells. Physiol. Zool. 69, 343–350.
Simonet Roda, M., Griesshaber, E., Ziegler, A., Rupp, U., Yin, X., Häussermann, V., Laudien, J., Brand, U., Eisenhauer, A., Checa, A.G., Schmahl, W.W., 2019. Calcite fibre formation in modern brachiopod shells. Sci. Rep. 9, 598.
Tambutté, S., Tambutté, E., Zoccola, D., Caminiti, N., Lotto, S., Moya, A., Allemand, D., Adkins, J., 2007. Characterization and role of carbonic anhydrase in the calcification process of the azooxanthellate coral *Tubastrea aurea*. Marine Biol. 151, 71–83.
Tambutté, S., Holocomb, M., Ferrier-Pagés, C., Reynaud, S., Tambutté, E., Zoccola, D., Allemand, D., 2011. Coral biomineralization: From the gene to the environment. J. Exp. Mar. Biol. Ecol. 408, 58–78.
Toyofuku, T., Matsuo, M.Y., De Nooijer, L.J., Nagai, Y., Kawada, S., Fujita, K., Reichart, G., Nomaki, H., Tsuchiya, M., Sakaguchi, H., Kitazato, H., 2017. Proton pumping accompanies calcification in foraminifera. Nat. Commun. 8, 14145.

Temereva, E.N., Kuzmina, T.V., 2017. The first data on the innervation of the lophophore in the rhynchonelliform brachiopod *Hemithiris psittacea*: what is the ground pattern of the lophophore in lophophorates? BMC Evol. Biol. 17, 1–12.
Veizer, J., Fritz, P., Jones, B., 1986. Geochemistry of brachiopods: Oxygen and carbon isotopic records of Paleozoic oceans. Geochim. Cosmochim. Acta 50, 1679–1696.
Wählisch, F.C., Peter, N.J., Abad, O.T., Oliveira, M.V., Schneider, A.S., Schmahl, W., Griesshaber, E., Bennewitz, R., 2014. Surviving the surf: The tribomechanical properties of the periostracum of Mytilus sp. Acta Biomater. 10, 3978–3985.
Walther, P., Ziegler, A., 2002. Freeze-substitution of high-pressure frozen samples: the visibility of biological membranes is improved when the substitution medium contains water. J. Microsc. 208, 3–10.
Walther, P., 2008. High-resolution cryoscanning electron microscopy of biological samples. In: Schatten, H., Pawley, J.B. (Eds.), Biological Low-Voltage Scanning Electron Microscopy. Springer, pp. 245–261. https://doi.org/10.1007/978-0-387-72972-5_10.
Weiner, S., Levi-kalisman, Y., Raz, S., Addadi, L., 2003. Biologically formed amorphous calcium carbonate. Connect. Tissue Res. 44, 214–218.
Weiner, S., Addadi, L., 2011. Crystallization pathways in biomineralization. Annu. Rev. Earth Planet. Sci. 41, 21–40.
Weiss, I.M., Tuross, N., Addadi, L., 2002. Mollusc larval shell formation: amorphous calcium carbonate is a precursor phase for aragonite. J. Exp. Zool. 293, 478–491.
Wefer, G., Berger, W.H., 1991. Isotope paleontology: growth and composition of calcareous species. Mar. Geol. 100, 207–248.
Wheatly, M.G., 1999. Calcium homeostasis in crustacea: the evolving role of branchial, renal, digestive and hypodermal epithelia. J. Exp. Zool. 283, 620–640.
Wheatly, M.G., Zhang, Z., Weil, J.R., Rogers, J.V., Stiner, L.M., 2001. Novel subcellular and molecular tools to study Ca^{2+} transport mechanisms during the elusive moultings stages of crustaceans: flow cytometry and polyclonal antibodies. J. Exp. Zool. 204, 959–966.
Wheatly, M.G., Gao, Y., Gillen, C.M., 2007. Paradox of epithelial cell calcium homeostasis during vectorial transfer in crayfish kidney. General. Comp. Endocrinol. 152, 267–272.
Williams, A., 1966. Growth and structure of the shell of living articulate brachiopod. Nature 211, 1146–1148.
Williams, A., 1968a. Evolution of the shell of structure of articulate brachiopods. Spec. Pap. Palaeontol. 2, 1–55.
Williams, A., 1968b. A history of skeletal secretion among articulate brachiopods. Lethaia 1, 268–287.
Williams, A., 1997. Shell structure. In: In: Kaesler, R.L. (Ed.), Treatise on Invertebrate Paleontology. Part H, Brachiopoda, vol. 1, Revised. Geological Society of America and University of Kansas, pp. 267–320.
Williams, A., Carlson, S.J., Brunton, C.H., 2000. Brachiopod classification. In: In: Kaesler, R.L. (Ed.), Treatise on Invertebrate Paleontology. Part H, Brachiopoda, vol. 2, Revised. Geological Society of America and University of Kansas, pp. 1–29.
Ye, F., Crippa, G., Angiolini, L., Brand, U., Capitani, G., Cusack, M., Garbelli, C., Griesshaber, E., Harper, E., Schmahl, W., 2018a. Mapping of recent brachiopod microstructure: a tool for environmental studies. J. Struct. Biol. 201, 221–236.
Ye, F., Crippa, G., Garbelli, C., Griesshaber, E., 2018b. Microstructural data of six recent brachiopod species: SEM, EBSD, morphometric and statistical analyses. Data Brief 18, 300–318.
Yin, X., Ziegler, A., Kelm, K., Hofmann, R., Watermeyer, P., Alexa, P., Villinger, C., Rupp, U., Schlüter, L., Reusch, T., Griesshaber, E., Schmahl, W.W., 2017. Formation and mosaicity of coccolith segment calcite of the marine algae *Emiliania huxleyi*. J. Phycol. 54, 85–104.
Yu, Z., Xie, L., Lee, S., Zhang, R., 2006. A novel carbonic anhydrase from the mantle of the pearl oyster (*Pinctada fucata*). Compar. Biochem. Physiol. Part B: Biochem. Mol. Biol. 143, 190–194.
Ziegler, A., 1997. Immunocytochemical localization of Na^+, K^+-ATPase in the calcium-transporting sternal epithelium of the terrestrial isopod *Porcellio scaber* Latr. (Crustacea). J. Histochem. Cytochem. 45, 437–446.
Ziegler, A., 2002. X-ray microprobe analysis of epithelial calcium transport. Cell Calcium 31, 307–321.
Ziegler, A., Weihrauch, D., Towle, D.W., Hagedorn, M., 2002. Expression of Ca^{2+}-ATPase and Na^+/Ca^{2+}-exchanger is upregulated during epithelial Ca^{2+} transport in hypodermal cells of the isopod *Porcellio scaber*. Cell Calcium 32, 131–141.
Ziegler, A., Weihrauch, D., Hagedorn, M., Towle, D.W., Bleher, R., 2004. Expression and polarity reversal of V-type H^+-ATPase during the mineralization-demineralization cycle in *Porcellio scaber* sternal epithelial cells. J. Exp. Biol. 207, 1749–1756.
Ziegler, A., Fabritius, H., Hagedorn, M., 2005. Microscopical and functional aspects of calcium-transport and deposition in terrestrial isopods. Micron 36, 137–153.
Ziegler, A., 2008. The cationic composition and pH in the moulting fluid of *Porcellio scaber* (Crustacea, Isopoda) during calcium carbonate deposit formation and resorption. J. Comparat. Physiol. B 178, 67–76.